A chromatic feature detector in the retina signals visual context changes

Larissa Höfling[1,2], Klaudia P. Szatko[1,2,9], Christian Behrens[1], Yuyao Deng[1,2], Yongrong Qiu[1,2], David A. Klindt[8], Zachary Jessen[5], Gregory W. Schwartz[5], Matthias Bethge[2,3], Philipp Berens[1,2,3,4], Katrin Franke[1,10], Alexander S. Ecker[6,7], and Thomas Euler[1,2,✉]

[1]Institute for Ophthalmic Research, University of Tübingen, Tübingen, Germany
[2]Centre for Integrative Neuroscience, University of Tübingen, Tübingen, Germany
[3]Tübingen AI Center, University of Tübingen, Tübingen, Germany
[4]Hertie Institute for AI in Brain Health, Tübingen, Germany
[5]Feinberg School of Medicine, Department of Ophthalmology, Northwestern University, Chicago, IL, USA
[6]Institute of Computer Science and Campus Institute Data Science, University of Göttingen, Göttingen, Germany
[7]Max Planck Institute for Dynamics and Self-Organization, Göttingen, Germany
[8]SLAC National Accelerator Laboratory, Stanford University, Menlo Park, CA, USA
[9]Current affiliation: National Institute of Neurological Disorders and Stroke, National Institutes of Health, Bethesda, MD, USA
[10]Current affiliation: Department of Neuroscience, Baylor College of Medicine, Houston, TX, USA

The retina transforms patterns of light into visual feature representations supporting behaviour. These representations are distributed across various types of retinal ganglion cells (RGCs), whose spatial and temporal tuning properties have been studied extensively in many model organisms, including the mouse. However, it has been difficult to link the potentially nonlinear retinal transformations of natural visual inputs to specific ethological purposes. Here, we discover a nonlinear selectivity to chromatic contrast in an RGC type that allows the detection of changes in visual context. We trained a convolutional neural network (CNN) model on large-scale functional recordings of RGC responses to natural mouse movies, and then used this model to search *in silico* for stimuli that maximally excite distinct types of RGCs. This procedure predicted centre colour-opponency in transient Suppressed-by-Contrast RGCs (tSbC), a cell type whose function is being debated. We confirmed experimentally that these cells indeed responded very selectively to Green-OFF, UV-ON contrasts. This type of chromatic contrast was characteristic of transitions from ground to sky in the visual scene, as might be elicited by head- or eye-movements across the horizon. Because tSbC cells performed best among all RGC types at reliably detecting these transitions, we suggest a role for this RGC type in providing contextual information (i.e. sky or ground) necessary for the selection of appropriate behavioural responses to other stimuli, such as looming objects. Our work showcases how a combination of experiments with natural stimuli and computational modelling allows discovering novel types of stimulus selectivity and identifying their potential ethological relevance.

retina | colour vision | computational modelling | digital twin | early visual pathway | natural stimuli

Correspondence: ***thomas.euler@cin.uni-tuebingen.de***

Introduction

Sensory systems evolved to generate representations of an animal's natural environment useful for survival and procreation (1). These environments are complex and high-dimensional, and different features are relevant for different species (reviewed in (2)). As a consequence, the representations are adapted to an animal's needs: features of the world relevant for the animal are represented with enhanced precision, whereas less important features are discarded. Sensory processing is thus best understood within the context of the environment an animal evolved in and that it interacts with (reviewed in (3, 4)).

The visual system is well-suited for studying sensory processing, as the first features are already extracted at its experimentally well-accessible front-end, the retina (reviewed in (2, 7)). In the mouse, this tissue gives rise to around 40 parallel channels that detect different features (6, 8–10), represented by different types of retinal ganglion cells (RGCs), whose axons send information to numerous visual centres in the brain (11). Some of these channels encode basic features, such as luminance changes and motion, that are only combined in downstream areas to support a range of behaviours such as cricket hunting in mice (12). Other channels directly extract specific features from natural scenes necessary for specific behaviours. For instance, transient OFF-α cells trigger freezing or escape behaviour in response to looming stimuli (13–15).

For many RGC types, however, we lack understanding of the features they encode and how these link to behaviour (16). One reason for this is that the synthetic stimuli commonly used to study retinal processing fail to drive retinal circuits "properly" and, hence, cannot uncover critical response properties triggered in natural environments. Colour, for example, is a salient feature in nature, and the mouse visual system dedicates intricate circuitry to the processing of chromatic information (17–22). Studies using synthetic stimuli have revealed nonlinear and centre-surround interactions between colour channels, but it is not clear how these are engaged in retinal processing of natural environments.

Indeed, stimuli capturing the statistics of natural environments have revealed a larger complexity in retinal spatial nonlinearities than had been previously described based on simpler synthetic stimuli (23). Such nonlinearities, crucial for the encoding of natural stimuli, cannot be captured by Linear-Nonlinear (LN) models of retinal processing, and several improvements over LN models have been proposed for the identification of receptive fields (RF) (reviewed in

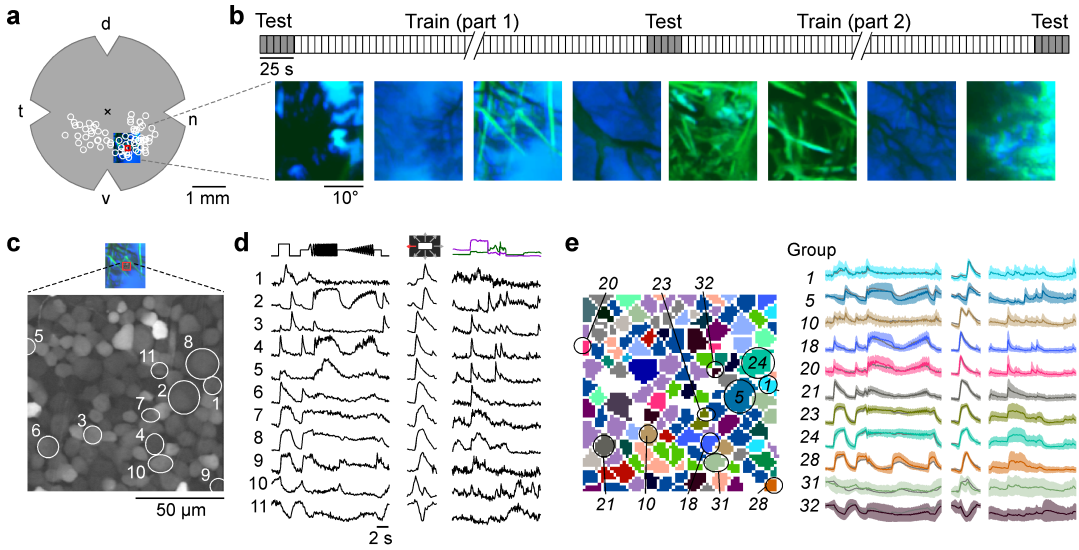

Figure 1. Mouse RGCs display diverse responses to a natural movie stimulus (a) Illustration of a flat-mounted retina, with recording fields (white circles) and stimulus area centred on the red recording field indicated (cross marks optic disc; d, dorsal; v, ventral; t, temporal; n, nasal). **(b)** Natural movie stimulus structure (top) and example frames (bottom). The stimulus consisted of 5-s clips taken from UV-green footage recorded outside (5), with 3 repeats of a 5-clip test sequence (highlighted in grey) and a 108-clip training sequence (see Methods). **(c)** Representative recording field (bottom; marked by red square in (a)) showing somata of ganglion cell layer (GCL) cells loaded with Ca^{2+} indicator OGB-1. **(d)** Ca^{2+} responses of exemplary RGCs (indicated by circles in (c)) to chirp (left), moving bar (centre), and natural movie (right) stimulus. **(e)** Same recording field as in (c) but with cells colour-coded by functional RGC group (left; see Methods and (6)) and group responses (coloured, mean ± SD across cells; trace of example cells in (d) overlaid in black).

(24)). In recent years, convolutional neural network (CNN) models have become the state-of-the-art approach for predictive modelling of visual processing, both in the retina (25–28), as well as in higher visual areas (29–31). In the cortex, two recent studies took the CNN modelling approach further, beyond response prediction, by probing the networks for stimuli that would maximally excite the modelled neurons (32, 33). The resulting *maximally exciting inputs* (MEIs) were more complex and diverse than expected based on previous results obtained with synthetic stimuli and linear methods. Leveraging the power of this approach, another study highlighted the ethological relevance of colour by uncovering a state-dependent shift in chromatic preference of mouse V1 neurons, a shift that could facilitate the detection of aerial predators against a UV-bright sky (34).

Here, we combined the power of CNN-based modelling with large-scale recordings from RGCs to investigate colour processing in the mouse retina under natural stimulus conditions. Since mouse photoreceptors are sensitive to green and UV light (35), we recorded RGC responses to stimuli capturing the chromatic composition of natural mouse environments in these two chromatic channels. A model-guided search for MEIs in chromatic stimulus space predicted a novel type of chromatic tuning in transient Suppressed-by-Contrast (tSbC) RGCs, a type whose function is being debated (36–38).

A detailed *in-silico* characterisation followed up by experimental validation *ex-vivo* confirmed this cell type's pronounced and unique selectivity for dynamic full-field changes from green-dominated to UV-dominated scenes, a type of visual input that matches the scene statistics of transitions across the horizon (5, 39, 40). We therefore suggest a role for tSbC RGCs in detecting behaviourally relevant changes in visual context, such as a transitions from ground (i.e. below the horizon) to sky (i.e. above the horizon).

Results

Here, we investigated colour processing in the mouse retina under natural stimulus conditions. To this end, we trained a CNN model on RGC responses to a movie covering both achromatic and chromatic contrasts occurring naturally in the mouse environment, and then performed a model-guided search for stimuli that maximise the responses of RGCs.

Mouse RGCs display diverse responses to a natural movie stimulus. Using two-photon population Ca^{2+} imaging, we recorded responses from 8,388 cells (in 72 recording fields across 32 retinae) in the ganglion cell layer (GCL) of the isolated mouse retina (Figure 1a) to a range of visual stimuli. Since complex interactions between colour channels have been mostly reported in the ventral retina and opsin-transitional zone, we focused our recordings on these regions (20, 21).

The stimuli included two achromatic synthetic stimuli – a contrast and frequency modulation ("chirp" stimulus) and a bright-on-dark bar moving in eight directions ("moving bar", MB) – to identify the functional cell type (see below), as well as a dichromatic natural movie (Figure 1b-d). The latter was composed of footage recorded outside in the field using a camera that captured the spectral bands (UV and green; (5)) to which mouse photoreceptors are sensitive ($\lambda^S_{peak} = 360, \lambda^M_{peak} = 510$ nm for S- and M-cones, respectively (35)). We used 113 different movie clips, each lasting 5 s, that were displayed in pseudo-random order. Five of these constituted the test set and were repeated three times: at the beginning, in the middle and at the end of the movie

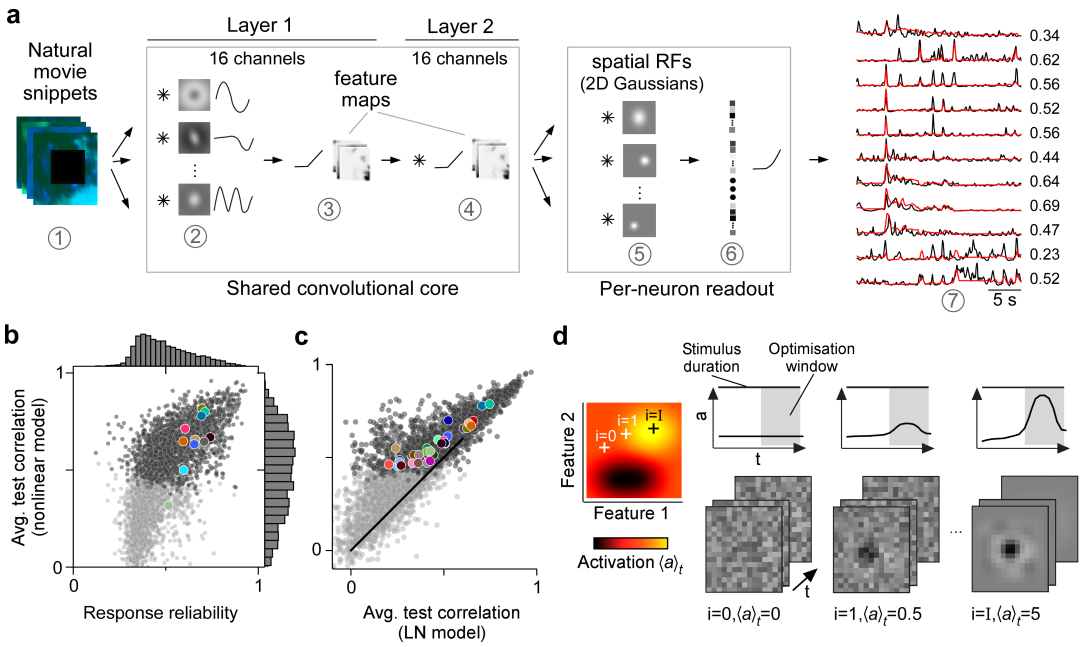

Figure 2. CNN model captures diverse tuning of RGC groups and predicts MEIs (a) Illustration of the CNN model and its output. The model takes natural movie clips as input (1), performs convolutions with 3D space-time separable filters (2) followed by a nonlinear activation function (3) in two consecutive layers (2-4) within its core, and feeds the output of its core into a per-neuron readout. For each RGC, the readout convolves the feature maps with a learned RF modelled as a 2D Gaussian (5), and finally feeds a weighted sum of the resulting vector through a softplus nonlinearity (6) to yield the firing rate prediction for that RGC (7). Numbers indicate averaged single-trial test set correlation between predicted (red) and recorded (black) responses. **(b)** Test set correlation between model prediction and neural response (averaged across three repetitions) as a function of response reliability (see Methods) for N=3,527 RGCs. Coloured dots correspond to example cells shown in Figure 1c-e. Dots in darker grey correspond to the N=1,947 RGCs that passed the model test correlation and movie response quality criterion (see Methods and Figure 1-figure supplement 1Ic). **(c)** Test set correlation (as in (b)) of model vs. test set correlation of a linearised version of the CNN model (for details, see Methods). Coloured dots correspond to RGC groups 1-32 (6). Dark and light grey dots as in (b). **(d)** Illustration of model-guided search for maximally exciting inputs (MEIs). The trained model captures neural tuning to stimulus features (far left; heat map illustrates "landscape´´ of neural tuning to stimulus features). Starting from a randomly initialised input (2nd from left; a 3D tensor in space and time; only one colour channel illustrated here), the model follows the gradient along the tuning surface (far left) to iteratively update the input until it arrives at the stimulus (bottom right) that maximises the model neuron's activation within an optimisation time window (0.66 s, grey box, top right).

presentation, thereby allowing to assess the reliability of neuronal responses across the recording (Figure 1b, top).

The responses elicited by the synthetic stimuli and the natural movie were diverse, displaying ON (Figure 1d, rows 4-9), ON-OFF (row 3) and OFF (rows 1 and 2), as well as sustained and transient characteristics (e.g., rows 8 and 4, respectively). Some responses were suppressed by temporal contrast (generally, rows 10, 11; at high contrast and frequency, row 9). A total of 6,984 GCL cells passed our response quality criteria (see Methods); 3,527 cells could be assigned to one of 32 previously characterised functional RGC groups (6) based on their responses to the chirp and moving bar stimuli using our recently developed classifier (Figure 1e; Figure 1-figure supplement 1Ia) (5). Cells assigned to any of groups 33-46 were considered displaced amacrine cells and were not analysed in this study (for detailed filtering pipeline, see Figure 1-figure supplement 1Ic).

CNN model captures diverse tuning of RGC groups and predicts MEIs. We trained a CNN model on the RGCs' movie responses (Figure 2a) and evaluated model performance as the correlation between predicted and trial-averaged measured test responses, $C(\hat{r}^{(n)}, \langle r^{(n)} \rangle_i)$ (Figure 2b). This metric can be interpreted as an estimate of the achieved fraction of the maximally achievable correlation (see Methods). The mean correlation per RGC group ranged from 0.32 (G_{14}) to 0.79 (G_{24}) (Figure 1-figure supplement 1Ib) and reached an average of 0.48 (for all N=3,527 cells passing filtering steps 1-3, Figure 1-figure supplement 1Ic). We also tested the performance of our nonlinear model against a linearised version (see Methods; equivalent to a Linear-Nonlinear (LN) model, and from here on "LN model") and found that the nonlinear CNN model achieved a higher test set correlation for all RGC groups (average correlation LN model: 0.38; G_{14}: 0.2, G_{24}: 0.65, Figure 2c).

Next, we wanted to leverage our nonlinear CNN model to search for potentially nonlinear stimulus selectivities of mouse RGC groups. Towards this goal, we aimed to identify stimuli that optimally drive RGCs of different groups. For linear systems, the optimal stimulus is equivalent to the linear filter and can be identified with classical approaches such as reverse correlation (41). However, since both the RGCs and the CNN model were nonlinear, a different approach was necessary. Other recent modelling studies in the visual system have leveraged CNN models to predict static maximally exciting inputs (MEIs) for neurons in monkey V4 (33, 42) and mouse V1 (32, 34). We adopted this approach to predict dynamic (i.e., time-varying) MEIs for mouse RGCs. We used gradient ascent on a randomly initialised, contrast- and range-constrained input to find the stimulus that maximised the mean activation of a given model neuron within a short time window (0.66 s; see Methods; Figure 2d).

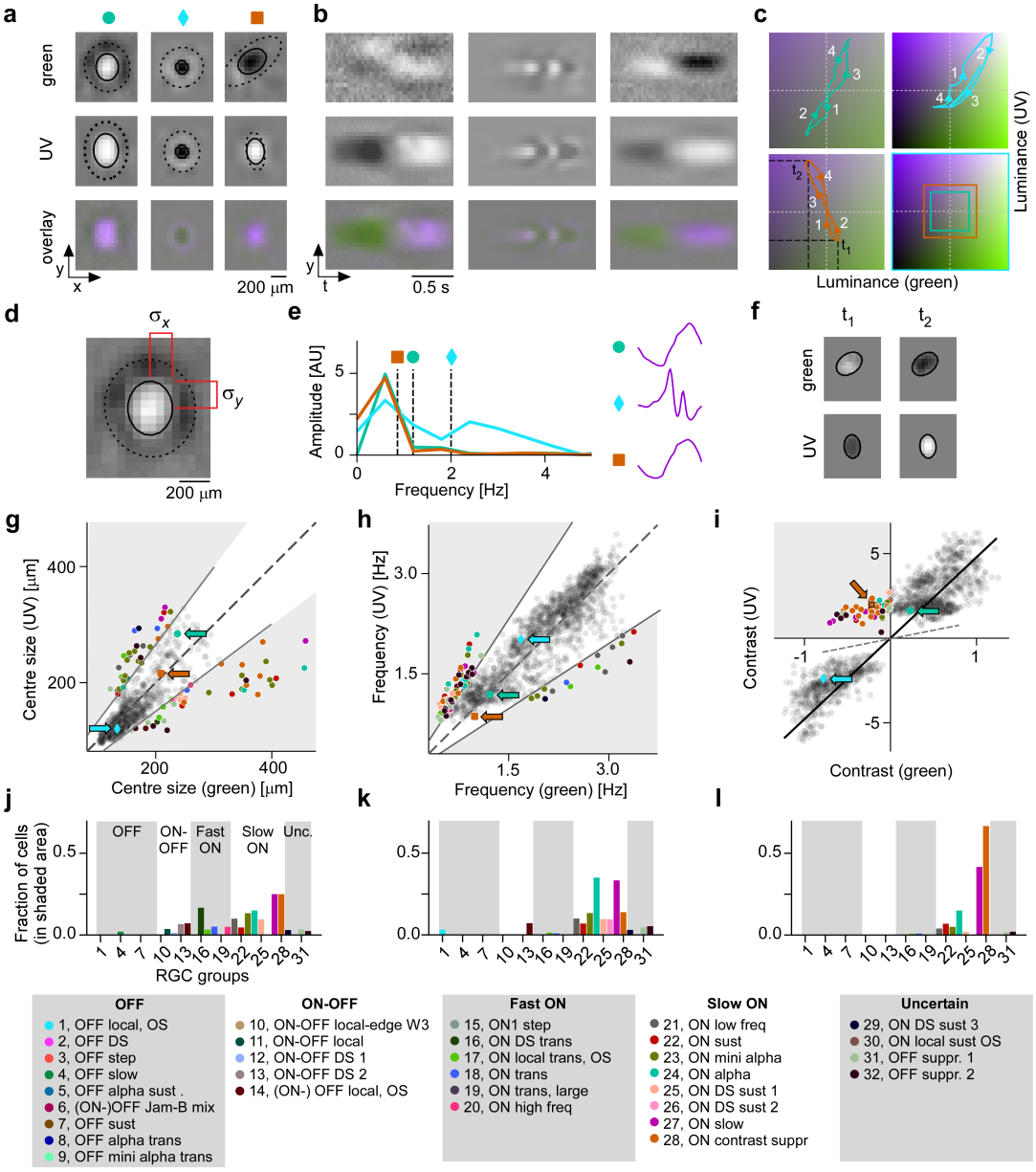

Figure 3. Spatial, temporal and chromatic properties of MEIs differ between RGC groups (a) Spatial component of three example MEIs for green (top), UV (middle) and overlay (bottom). Solid and dashed circles indicate MEI centre and surround fit, respectively. For display, spatial components s in the two channels were re-scaled to a similar range and displayed on a common grey-scale map ranging from black for $-max(|s|)$ to white for $max(|s|)$, i.e. symmetric about 0 (grey). **(b)** Spatio-temporal (y-t) plot for the three example MEIs (from (a)) at a central vertical slice for green (top), UV (middle) and overlay (bottom). Grey-scale map analogous to (a). **(c)** Trajectories through colour space over time for the centre of the three MEIs. Trajectories start at the origin (grey level); direction of progress indicated by arrow heads. Bottom right: Bounding boxes of the respective trajectory plots. **(d)** Calculation of MEI centre size, defined as $\sigma_x + \sigma_y$, with σ_x and σ_y the s.d. in horizontal and vertical direction, respectively, of the DoG fit to the MEI. **(e)** Calculation of MEI temporal frequency: Temporal components are transformed using Fast Fourier Transform, and MEI frequency is defined as the amplitude-weighted average frequency of the Fourier-transformed temporal component. **(f)** Calculation of centre contrast, which is defined as the difference in intensity at the last two peaks (indicated by t_1 and t_2, respectively, in (c)). For the example cell (orange markers and lines), green intensity decreases, resulting in OFF contrast, and UV intensity increases, resulting in ON contrast. **(g)** Distribution of green and UV MEI centre sizes across N=1,613 cells (example MEIs from (a-c) indicated by arrows; symbols as shown on top of (a)). 95% of MEIs were within an angle of $\pm 8°$ of the diagonal (solid and dashed lines); MEIs outside of this range are coloured by cell type. **(h)** As (g) but for distribution of green and UV MEI temporal frequency. 95% of MEIs were within an angle of $\pm 11.4°$ of the diagonal (solid and dashed lines). **(i)** As (g) but for distribution of green and UV MEI centre contrast. MEI contrast is shifted away from the diagonal (dashed line) towards UV by an angle of 33.2° due to the dominance of UV-sensitive S-opsin in the ventral retina. MEIs at an angle $> 45°$ occupy the upper left, colour-opponent (UV^{ON}-$green^{OFF}$) quadrant. **(j, k)** Fraction of MEIs per cell type that lie outside the angle about the diagonal containing 95% of MEIs for centre size and temporal frequency. Broad RGC response types indicated as in (6). **(l)** Fraction of MEIs per cell type in the upper-left, colour-opponent quadrant for contrast.

It is important to note that MEIs should not be confused with or interpreted as the linear filters that result from classical approaches (e.g., reverse correlation). This is because they result from an optimisation procedure that aims at predicting the *optimal* stimulus for a cell. In fact, they can differ significantly from linear filters, for example by exhibiting more complexity and higher frequency components (32).

MEIs reflect known functional RGC group properties. The resulting MEIs were short, dichromatic movie clips; their spatial, temporal, and chromatic properties and interactions thereof are best appreciated in lower-dimensional visualisations (Figure 3a–c; more example MEIs in Figure 3-figure supplement 1II).

To analyse the MEIs in terms of these properties, we decomposed them into their spatial and temporal components, separately for green and UV, and parameterised the spatial component as a Difference-of-Gaussians (DoG) (40) (N=1,613 out of 1,947, see Methods). We then located MEIs along the axes in stimulus space corresponding to three properties: centre size, mean temporal frequency, and centre contrast, separately for green and UV (Figure 3d-f). These MEI properties reflect RGC response properties classically probed with synthetic stimuli, such as spots of different sizes (8), temporal frequency modulations (6), and stimuli of varying chromatic contrast (20, 21). Using the MEI approach, we were able to reproduce known properties of RGC groups (Figure 3g-i). For example, sustained ON α RGCs (G_{24}), which are known to prefer large stimuli (6, 36), had MEIs with large centres (G_{24}, N=20 cells: green centre size, mean $\pm$ SD: 195 $\pm 82\,\mu$m; UV centre size $178 \pm 45\,\mu$m; average across all RGC groups: green $148 \pm 42\,\mu$m, UV $141 \pm 42\,\mu$m; see Figure 3g).

The MEI's temporal frequency relates to the temporal frequency preference of an RGC: MEIs of G_{20} and G_{21}, termed ON high frequency and ON low frequency (6), had high and low average temporal frequency, respectively (G_{20}, N=40 cells, green, mean $\pm$ SD: 2.71 ± 0.16 Hz, UV 2.86 ± 0.22 Hz; G_{21}, N=50 cells, green, mean $\pm$ SD: 2.32 ± 0.63 Hz, UV 1.98 ± 0.5 Hz; see Figure 3h). Some MEIs exhibit fast oscillations (Figure 3e and Figure 3-figure supplement 1II). This is not an artefact but rather a consequence of optimising a stimulus to maximise activity over a 0.66 s time window (Figure 2d). To maximise the response of a transient RGC over several hundred milliseconds, it has to be stimulated repetitively, hence the oscillations in the MEI. Maximising the response over a shorter time period results in MEIs without oscillations (Figure 3-figure supplement 2III).

Finally, the contrast of an MEI reflects what is traditionally called a cell's ON vs. OFF preference: MEIs of ON and OFF RGCs had positive and negative contrasts, respectively (Figure 3i). An ON-OFF preference can be interpreted as a tuning map with two optima – one in the OFF- and one in the ON-contrast regime. For an ON-OFF cell, there are hence two stimuli that are approximately equally effective at eliciting responses from that cell. Consequently, for the ON-OFF RGC groups, optimisation resulted in MEIs with ON or OFF contrast, depending on the relative strengths of the two optima and on the initial conditions (Figure 3-figure supplement 1II, G_{10}, and see Discussion).

MEIs were also largely consistent within functional RGC groups (Figure 3-figure supplement 1II). Where this was not the case, the heterogeneity of MEIs could be attributed to a known heterogeneity of cells within that group. For example, MEIs of G_{31} RGCs were diverse (Figure 3-figure supplement 1II), and the cells that were originally grouped to form G_{31} probably spanned several distinct types, as suggested by the group's unusually high coverage factor (6). Together, these results provided strong evidence that RGCs grouped based on responses to synthetic stimuli (chirp and MB) also form functional groups in natural movie response space.

CNN model predicts centre colour-opponency in RGC group G_{28}. Our goal was to explore chromatic tuning of RGCs and to identify novel stimulus selectivities related to chromatic contrast. Therefore, we specifically focused on regions in stimulus space where a given stimulus property differs for green and UV. Therefore, for centre size and temporal frequency, we asked, which RGC groups contributed to the MEIs outside of the 95$^{\text{th}}$ percentile around the diagonal (Figure 3g,h,j,k). These 5% MEIs furthest away from the diagonal were almost exclusively contributed by ON cells; and among these, more so by slow than by fast ON cells.

MEI contrast needed to be analysed differently than size and temporal frequency for two reasons. First, due to the dominance of UV-sensitive S-opsin in the ventral retina (17), stimuli in the UV channel were much more effective at eliciting RGC responses. As a result, the contrast of most MEIs is strongly shifted towards UV (Figure 3i). Second, contrast in green and UV can not only vary along positive valued axes (as is the case for size and temporal frequency), but can also take on opposite signs, resulting in colour-opponent stimuli. Whereas most MEIs had the same contrast polarity in both colour channels (i.e. both ON or OFF, Figure 3c, blue and turquoise trajectories), some MEIs had opposing contrast polarities in UV and green (Figure 3c, orange trajectory, and Figure 3i, upper left quadrant). Thus, for contrast, we asked which RGC groups contributed to colour-opponent MEIs (i.e. MEIs in the colour-opponent, upper left or lower right quadrant in Figure 3i). Again, slow ON RGCs made up most of the cells with colour-opponent MEIs. Here, G_{28} stood out: 66% (24/36) of all cells of this group had colour-opponent MEIs (UV^{ON}-$\text{green}^{\text{OFF}}$), followed by G_{27} with 42% colour-opponent MEIs.

The colour-opponency we found in G_{28} was not centre-surround, as described before in mice (20), but rather a centre-opponency ("co-extensive" colour-opponent RF; reviewed in (43)), as can be seen in the lower-dimensional visualisations (Figure 3a,b, right column; 3c, orange trajectory).

In conclusion, our model-guided *in-silico* exploration of chromatic stimulus space revealed a variety of preferred stimuli that captured known properties of RGC groups,

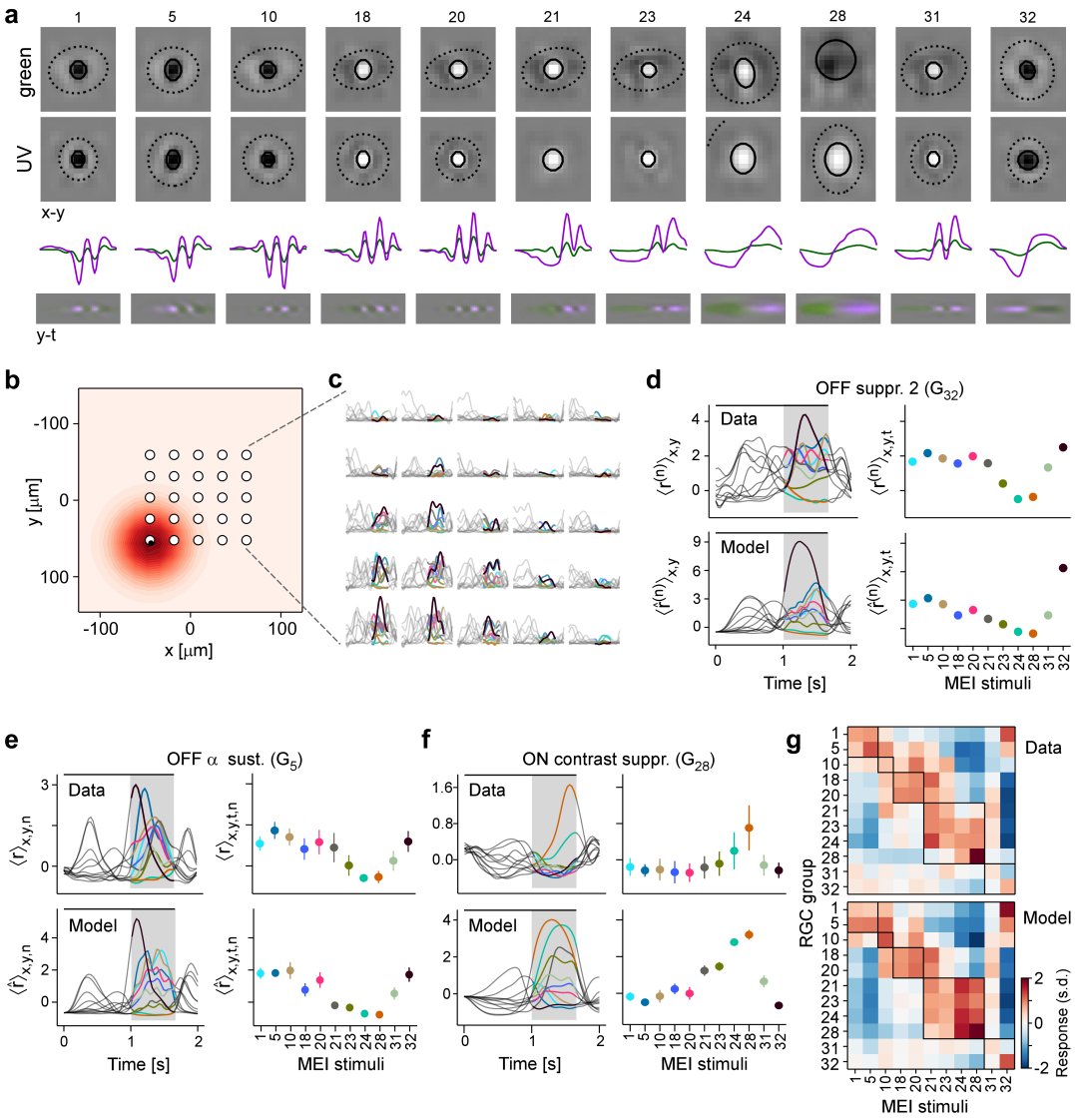

Figure 4. Experiments confirm MEIs predicted by model (a) MEIs shown during the experiment, with green and UV spatial components (top two rows), as well as green and UV temporal components (third row) and a spatio-temporal visualisation (fourth row). For display, spatial components s in the two channels were re-scaled to a similar range and displayed on a common grey-scale map ranging from black for $-max(|s|)$ to white for $max(|s|)$, i.e. symmetric about 0 (grey). Relative amplitudes of UV and green are shown in the temporal components. **(b)** Illustration of spatial layout of MEI experiment. White circles represent 5×5 grid of positions where MEIs were shown; red shading shows an example RF estimate of a recorded G_{32} RGC, with black dot indicating the RF centre position (Methods). **(c)** Responses of example RGC from (b) to the 11 different MEI stimuli at 25 different positions. **(d)** Recorded (top, $r^{(n)}$) and predicted (bottom, $\hat{r}^{(n)}$) responses to the 11 different MEIs for example RGC n from (b, c). Left: responses are averaged across the indicated dimensions x, y (different MEI locations); black bar indicates MEI stimulus duration (from 0 to 1.66 s), grey rectangle marks optimisation time window (from 1 to 1.66 s). Right: Response to different MEIs, additionally averaged across time (t; within optimisation time window). **(e,f)** Same as in (d), but additionally averaged across all RGCs (n) of G_5 (N=6) (e) and of G_{28} (N=12) (f). Error bars show SD across cells. **(g)** Confusion matrix, each row showing the z-scored response magnitude of one RGC group (averaged across all RGCs of that group) to the MEIs in (a). Confusion matrix for recorded cells (top; "Data") and for model neurons (bottom; "Model"). Black squares highlight broad RGC response types according to (6): OFF cells, ($G_{1,5}$) ON-OFF cells (G_{10}), fast ON cells ($G_{18,20}$), slow ON ($G_{21,23,24}$) and ON contrast suppressed (G_{28}) cells, and OFF suppressed cells ($G_{31,32}$).

and revealed a preference of G_{28} RGCs for centre colour-opponent, UV^{ON}-$green^{OFF}$ stimuli, a feature previously unknown for this RGC group.

Experiments confirm selectivity for chromatic contrast. Next, we verified experimentally that the MEIs predicted for a given RGC group actually drive cells of that group optimally. To this end, we performed new experiments in which we added to our battery of stimuli a number of MEIs chosen according to the following criteria: We wanted the MEIs to (*i*) span the response space (ON, ON-OFF, OFF, transient, sustained, and contrast-suppressed) and (*ii*) to represent both well-described RGC types, such as α cells (i.e. $G_{5,24}$), as well as poorly understood RGC types, such as suppressed-by-contrast cells ($G_{28,31,32}$) (Figure 4a). We therefore chose MEIs of RGCs from groups G_1 (OFF local), G_5 (OFF α sustained), G_{10} (ON-OFF local-edge), G_{18} (ON transient), G_{20} (ON high frequency), G_{21} (ON low frequency), G_{23} (ON mini α), G_{24} (sustained ON α), G_{28} (ON contrast suppressed), G_{31} (OFF suppressed 1), and G_{32} (OFF suppressed 2). For simplicity, in the following we refer to the MEI of an RGC belonging to group g as group g's MEI, or MEI g.

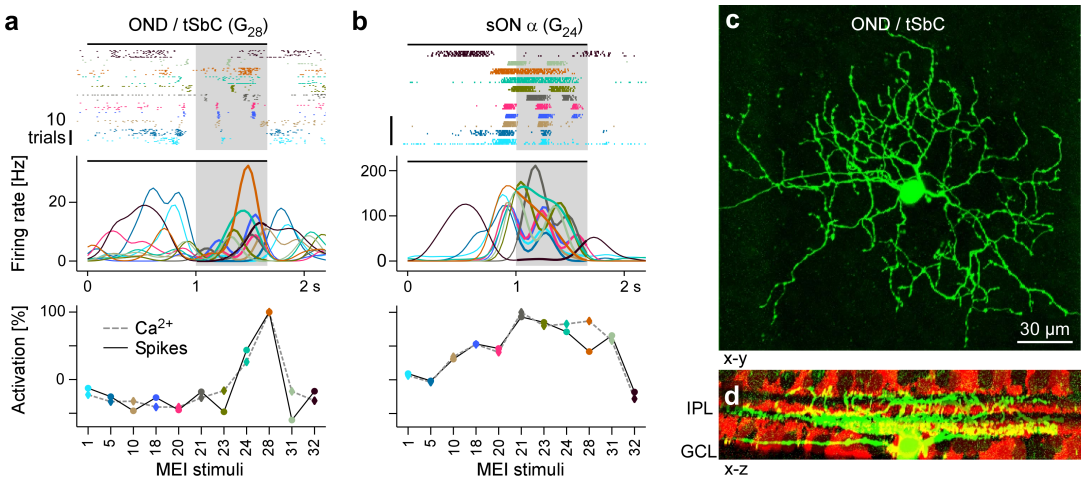

Figure 5. Electrical single-cell recordings of responses to MEI stimuli confirm chromatic selectivity of tSbC RGCs. (a) Spiking activity (top, raster plot; middle, firing rate) of a OND RGC in response to different MEI stimuli (black bar indicates MEI stimulus duration; grey rectangle marks optimisation time window, from 1 to 1.66 s). Bottom: Activation relative to mean as a function of MEI stimulus, averaged across cells (solid line, from electrical recordings, N=4; dashed line, from Ca^{2+} imaging, N=11 cells). Colours as in Figure 4. **(b)** Like (a) but for a sustained ON α cell (G_{24}; N=4 cells, both for electrical and Ca^{2+} recordings). **(c)** Different ON delayed (OND/tSbC, G_{28}) RGC (green) dye-loaded by patch pipette after cell-attached electrophysiology recording (z-projection; x-y plane). **(d)** Cell from (c, green) as side-projection (x-z), showing dendritic stratification pattern relative to choline-acetyltransferase (ChAT) amacrine cells (tdTomato, red) within the inner plexiform layer (IPL).

We presented these MEIs on a regularly spaced 5×5 grid to achieve approximate centring of stimuli on RGC RFs in the recording field (Figure 4b,c). For these recordings, we fit models whose readout parameters allowed us to estimate the RGCs' RF locations. We used these RF location estimates to calculate a spatially weighted average of the responses to the MEIs displayed at different locations, weighting the response at each location proportional to the RF strengths at those locations (Figure 4b, red highlight, and Figure 4d, top). We then performed the same experiment *in-silico*, confirming that the model accurately predicts responses to the MEIs (Figure 4d, bottom; Figure 4-figure supplement 1IV). These experiments allowed us to evaluate MEI responses at the RGC group level (Figure 4e–f; Figure 3-figure supplement 1 II).

We expected RGCs to show a strong response to their own group's MEI, a weaker response to the MEIs of functionally related groups, and no response to MEIs of groups with different response profiles. Indeed, most RGC groups exhibited their strongest ($G_{5,20,21,28,32}$) or second-strongest ($G_{1,10,23}$) response to their own group's MEI (Figure 4g, top). Conversely, RGC groups from opposing regions in response space showed no response to each others' MEIs (e.g. $G_{1,5}$ (OFF cells) vs. $G_{21\text{-}28}$ (slow ON cells)). The model's predictions showed a similar pattern (Figure 4g, bottom), thereby validating the model's ability to generalise to the MEI stimulus regime.

Notably, G_{28} RGCs responded very selectively to their own MEI 28, displaying only weak responses to most other MEIs (Figure 4f,g, selectivity index G_{28} to MEI 28 $SI_{G_{28}}(28)$ defined as the average difference in response between MEI 28 and all other MEIs in units of standard deviation of the response, mean $\pm$ SD: 2.58 ± 0.76; see Methods). This was in contrast to other RGC groups, such as G_{23} and G_{24}, that responded strongly to MEI 28, but also to other MEIs from the slow ON response regime (Figure 4g, top; Figure 4-figure supplement 1 IV, $SI_{G_{23}}(28)$, mean $\pm$ SD: 1.04 ± 0.69, $SI_{G_{24}}(28)$, mean $\pm$ SD: 1.01 ± 0.46). Hence, our validation experiments confirm the model's prediction that RGC group G_{28} is selective for centre colour-opponent, UV^{ON}-$green^{OFF}$ stimuli.

G_{28} corresponds to the transient Suppressed-by–Contrast RGC type. Next, we sought to identify which RGC type G_{28} corresponds to. In addition to its unique centre colour-opponency, the responses of G_{28} displayed a pronounced transient suppression to temporal contrast modulations (cf. chirp response in Figure 1e). Therefore, we hypothesised that G_{28} corresponds to the transient Suppressed-by-Contrast (tSbC) RGC type (37, 38, 44), which is one of three retinal SbC RGC types identified so far and is also referred to as ON delayed (OND) cell because of its delayed response onset (45).

To test this hypothesis, we performed cell-attached electrophysiology recordings (Figure 5) targeting tSbC/OND cells (N=4), identified by their responses to spots of multiple sizes (8), and later confirmed by their distinctive morphology ((45); type 73 in (9)) (Figure 5c,d). We recorded spikes while presenting the MEI stimuli (Figure 5a, top). Just like G_{28} RGCs in the Ca^{2+} imaging, tSbC/OND cells exhibited a pronounced selectivity for MEI 28, and were suppressed by most other MEIs (Figure 5a, middle and bottom). Notably, the characteristic delayed response onset was visible in both the Ca^{2+} (Figure 4f, top) and electrical (Figure 5a) responses but was not predicted by the model (Figure 4f, bottom).

As a control, we also recorded MEI responses of a different, well-characterised RGC type, sustained (s) ON α (G_{24}; (46)) (Figure 5b, top; N=4). Again, the electrical recordings of the cells' MEI responses yielded virtually the same results as the Ca^{2+} imaging (Figure 5b, middle and bottom; cf. Figure 4-figure supplement 1IV). Crucially, sON α cells were not selective for MEI 28. The fact that

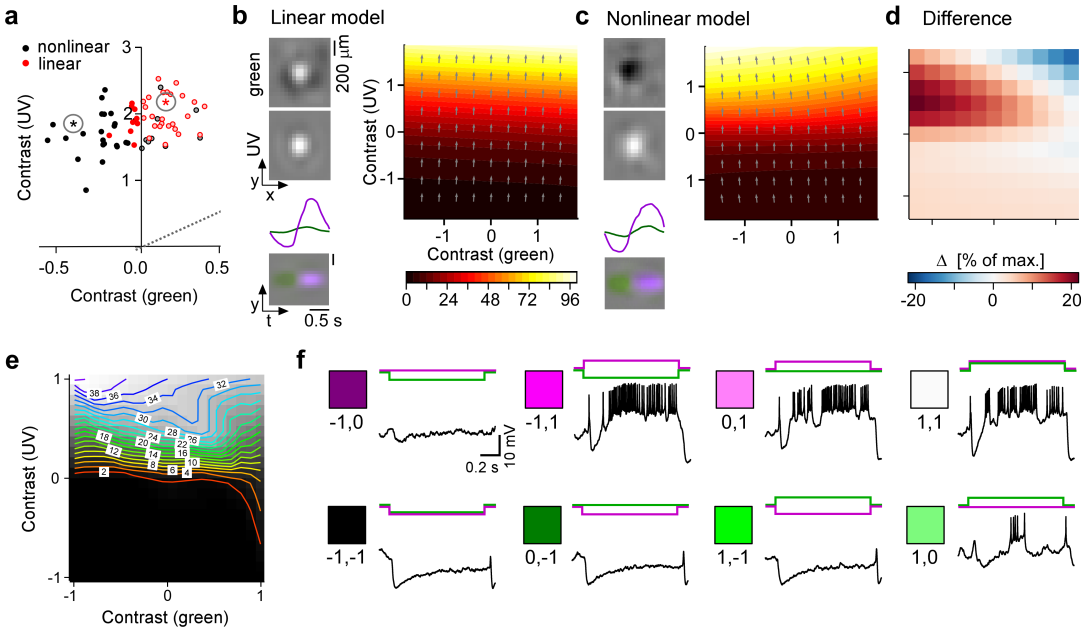

Figure 6. Chromatic contrast selectivity of G_{28} RGCs derives from a nonlinear transformation of stimulus space (a) Distribution of green and UV MEI centre contrast for a linear-nonlinear (LN) model (red) and a nonlinear CNN model (black). Colour-opponent cells highlighted by filled marker. **(b,c)** Left: MEIs for an example cell of RGC group G_{28}, generated with the LN model (b) or the CNN model (c). The cell's MEI centre contrast for both models is marked in (a) by asterisks. Right: Respective tuning maps of example model neuron in chromatic contrast space. Colours represent responses in % of maximum response; arrows indicate the direction of the response gradient across chromatic contrast space. **(d)** Difference in response predicted between LN and CNN model (in % of maximum response). **(e)** Contour plot of activity vs. green and UV contrast for an example tSbC (G_{28}) RGC measured in whole-cell current-clamp mode. Labels on the contour plot indicate spike count along isoresponse curves. **(f)** Traces are examples of responses at the 8 extremes of -100%, 0, or 100% contrast in each colour channel.

these experiments with precise positioning of stimuli on the cells' RFs elicited the same responses as the 2P experiments confirms the validity of the grid-approach for stimulus presentation used in the latter.

Chromatic contrast selectivity derives from a nonlinear transformation of stimulus space. Next, we asked whether G_{28} (tSbC) RGC's selectivity is a linear feature, as could be achieved by two linear filters with opposite signs for the two colour channels, or whether it is a nonlinear feature. To address this question, we tested whether an LN model (implemented using convolutions; see Methods) could recover the chromatic selectivity of G_{28} by predicting MEIs using the LN model (Figure 6). We found that the LN model predicted colour-opponent MEIs for only 9 out of 36 (25%) G_{28} RGCs (nonlinear CNN: 24 out of 36 (66%) colour-opponent MEIs; Figure 6a-c). This finding argues against the possibility that G_{28}'s colour opponency can be explained on the computational level by two opposite-sign linear filters operating on the two colour channels, which could be recovered by a LN model. Instead, it suggests the presence of a nonlinear dependency between chromatic contrast (of the stimulus) and chromatic selectivity (of the cell). In other words, G_{28} RGCs process stimuli differently depending on their chromatic contrast, a nonlinear feature that cannot be accurately captured by a LN model that makes a single estimate of the linear filter for the whole stimulus space.

To understand the nature of this dependency, we expanded the estimate of the model RGCs' tuning to colour contrast around the maximum (the MEI). We did this by mapping the model neurons' response and its gradient in 2D chromatic contrast space (Figure 6c). This analysis revealed that, indeed, G_{28} RGCs have a nonlinear tuning for colour contrast: they are strongly UV-selective at lower contrasts, but become colour-opponent, i.e. additionally inhibited by green, for higher contrasts. For individual neurons with very strong colour-opponency that extends over a large region of chromatic contrast space, also the LN model's approximation reflects this colour-opponency, which demonstrates that the LN model can in principle model colour-opponency, too (Figure 5-figure supplement 1V). We confirmed the model's predictions about G_{28}'s nonlinear tuning for colour contrast experimentally by electrically recording from morphologically identified G_{28} (tSbC) RGCs (Figure 6e,f). The example cell shown in the figure exhibits the same nonlinear tuning in chromatic contrast space, with the firing rate (Figure 6f) and, consequently, the tuning curve (Figure 6e) peaking for UV^{ON}-$green^{OFF}$ stimuli.

The nonlinearity in tuning to colour contrast of G_{28} RGCs leads to a warping of stimulus space (Figure 6) that amplifies the distance of colour-opponent stimuli from non-colour-opponent stimuli and thereby increases their discriminability. We therefore hypothesised that the representation of visual input formed by G_{28} might serve to detect an ethologically relevant, colour-opponent feature from the visual scene. What may be this feature?

Warped representation allows for detection of ground-to-sky transitions. Studies analysing visual scenery from the mouse's perspective have repeatedly found that chromatic contrast changes strongly at the

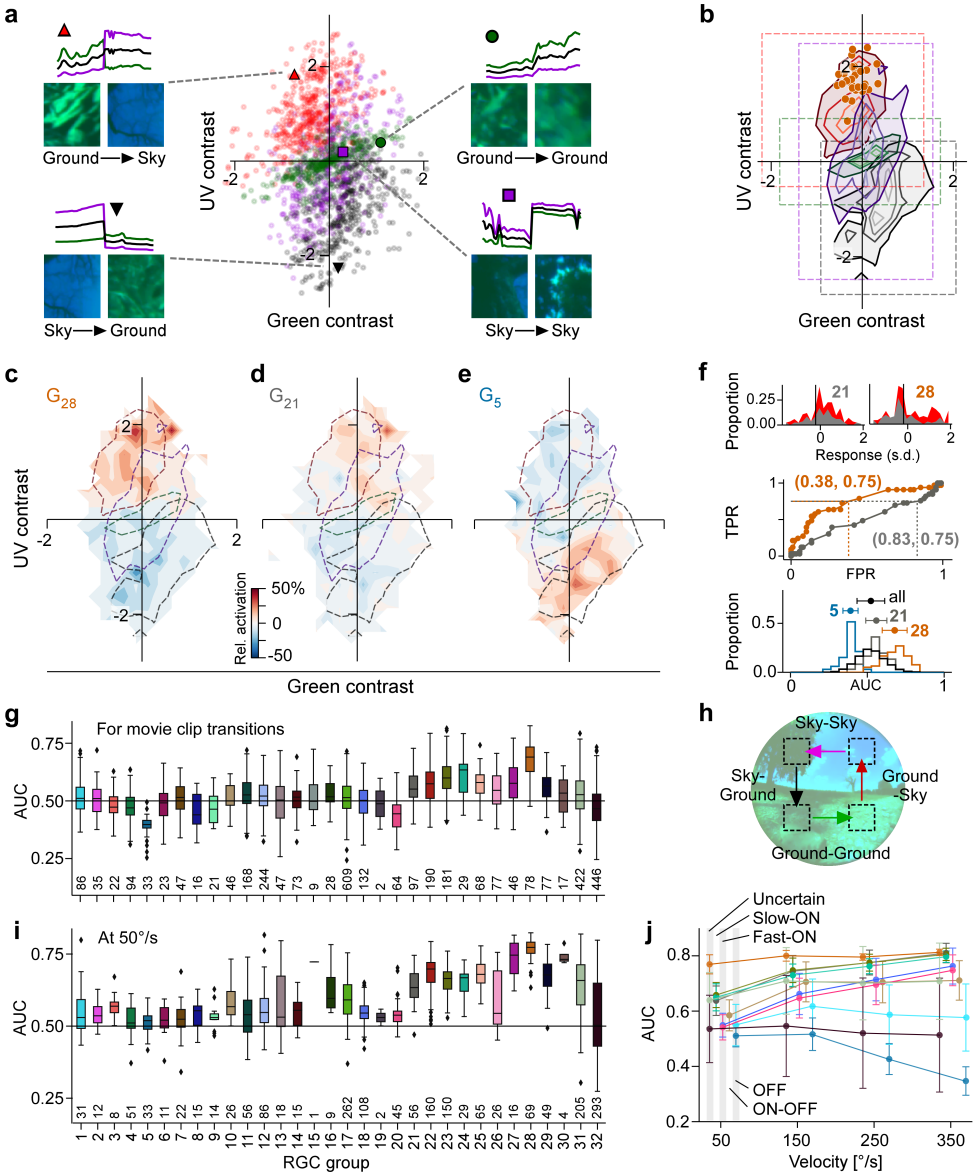

Figure 7. Chromatic contrast tuning allows detection of ground-to-sky transitions (a) Distribution of green and UV contrasts of all movie inter-clip transitions (centre), separately for the 4 transition types, for each of which an example is shown: ground-to-sky (N=525, top left, red triangle), ground-to-ground (N=494, top right, green disk), sky-to-ground (N=480, bottom left, black downward triangle), and sky-to-sky (N=499, bottom right, purple square). Images show last and first frame of pre- and post-transition clip, respectively. Traces show mean full-field luminance of green and UV channels in last and first 1 s of pre- and post-transition clip. Black trace shows luminance averaged across colour channels. **(b)** Distributions as in (a), but shown as contours indicating isodensity lines of inter-clip transitions in chromatic contrast space. Density of inter-clip transitions was estimated separately for each type of transition from histograms within 10 $\times$ 10 bins that were equally spaced within the coloured boxes. Four levels of isodensity for each transition type shown, with density levels at 20 % (outermost contour, strongest saturation), 40 %, 60 % and 80 % (innermost contour, weakest saturation) of the maximum density observed per transition: 28 sky-to-ground (black), 75 ground-to-ground (green), 42 sky-to-sky (purple) and 45 ground-to-sky (red) transitions per bin. Orange markers indicate locations of N=36 G_{28} MEIs in chromatic contrast space (cf. Figure 3i). **(c)** Tuning map of G_{28} RGCs (N=78), created by averaging the tuning maps of the individual RGCs, overlaid with outermost contour lines from (b) (cf. Figure 6-figure supplement 2VIIb). **(d,e)** Same as (c) for G_{21} ((g), N=97) and G^5 ((h), N=33). **(f)** *Top*: Illustration of ROC analysis for two RGCs, a G_{21} (left) and a G_{28} (right). For each RGC, responses to all inter-clip transitions were binned, separately for ground-to-sky (red) and all other transitions (grey). *Middle*: Sliding a threshold d across the response range, classifying all transitions with response $> d$ as ground-to-sky, and registering the false-positive-rate (FPR) and true-positive-rate (TPR) for each threshold yields an ROC curve. Numbers in brackets indicate (FPR, TPR) at the threshold indicated by vertical line in histograms. *Bottom*: Performance for each cell, quantified as area under the ROC curve (AUC), plotted as distribution across AUC values for all cells (black), G_{21} (grey), G_5 (blue), and G_{28} (orange); AUC mean $\pm$ SD indicated as dots and horizontal lines above histograms. **(g)** Boxplot of AUC distributions per cell type. The box extends from the first quartile (Q_1) to the third quartile (Q_3) of the data; the line within a box indicates the median. The whiskers extend to the most extreme points still within $[Q_1 - 1.5 \times \text{IQR}, Q_3 + 1.5 \times \text{IQR}]$, IQR = inter-quartile range. Diamonds indicate points outside this range. All elements of the plot (upper and lower boundaries of the box, median line, whiskers, diamonds) correspond to actual observations in the data. Numbers of RGCs for each type are indicated in the plot. **(h)** Illustration of stimulus with transitions as in (a) but at different velocities (50, 150, 250, and 350°/s). **(i)** Like (g) but for model cells and transition movies from (h) at 50°/s. **(j)** AUC as function of transition velocity for example RGC groups ($G_{(1,5),\ (10),\ (18,20),\ (21,\ 23,\ 24),\ (28,\ 31,\ 32)}$).

horizon (5, 21, 39, 40). G_{28} RGCs are selective to this kind of change in chromatic contrast: their MEI consists of a spatially extensive and sustained change in luminance from green to UV. We hypothesised that this change in chromatic contrast might serve as a proxy for detecting changes in visual context, as might be elicited when a cell's RF transitions across the horizon. Such transitions could be caused by head or eye movements, and detecting this change in visual context (i.e. ground vs. sky) may help interpreting signals in other RGC channels.

To test if G_{28} (tSbC) RGCs respond to such a stimulus, we used the transitions between movie clips (*inter-clip transitions*; cf. Figure 1b) as a proxy for the type of visual input elicited by head or eye movements: ground-to-ground and sky-to-sky transitions for horizontal movements without change in visual context, and ground-to-sky and sky-to-ground transitions for vertical movements with a change in visual context. We then calculated the contrast of these transitions in the green and UV channel and mapped them to the chromatic contrast stimulus space (Figure 7a). We found that ground-to-ground and sky-to-sky transitions were distributed along the diagonal, whereas the two transitions resembling visual input elicited by vertical movements crossing the horizon fell into the two colour-opponent quadrants: sky-to-ground transitions in the lower right quadrant, and ground-to-sky transitions in the upper left quadrant (Figure 7a,b). The UV^{ON}-$green^{OFF}$ MEIs 28 share a location in stimulus space with ground-to-sky transitions in terms of chromatic contrast (cf. Fig 3i).

Do G_{28} RGCs indeed respond strongly to visual context changes as occur in ground-to-sky transitions, i.e. to the "naturally occurring version" of their MEIs? To address this question, we extracted the RGC responses to the inter-clip transitions, thereby mapping out their tuning across chromatic contrasts (Figure 6-figure supplement 1VI, Figure 6-figure supplement 6VIIb), and then averaged the resulting single-cell tuning maps for each RGC group (for examples, see Figure 7c-e). G_{28} is most strongly tuned to full-field transitions in the upper left quadrant containing mostly ground-to-sky inter-clip transitions (Figure 7c) – unlike, for example, non-colour-opponent reference RGC groups from the slow ON and OFF response regime (Figure 7d,e).

Could a downstream visual area detect ground-to-sky visual context changes based on input from G_{28} RGCs? To answer this question, we performed a linear detection analysis for each RGC by sliding a threshold across its responses to the inter-clip transitions, classifying all transitions that elicited an above-threshold response as ground-to-sky, and evaluating false-positive and true-positive rates (FPR and TPR, respectively) for each threshold (Figure 7f). Plotting the resulting TPRs for all thresholds as a function of FPRs yields a receiver operating characteristic (ROC) curve (47) (Figure 7f, middle). The area under this curve (AUC) can be used as a measure of detection performance: it is equivalent to the probability that a given RGC will respond more strongly to a ground-to-sky transition than to any other type of transition. Indeed, G_{28} RGCs achieved the highest AUC on average (Figure 7f, bottom, and g; G_{28}, mean $\pm$ SD AUC (N=78 cells): 0.68 ± 0.08; two-sample permutation test G_{28} vs. all other groups with at least N=4 cells (see Methods), significant for each group, with $\alpha = 0.0017$ Bonferroni-corrected for 30 multiple comparisons).

Ground-to-sky transitions and, therefore visual context changes, can also appear in the lower visual field, that is, on the dorsal retina, where RGCs receive weaker UV input (20). Therefore, we recorded additional fields in the dorsal retina (Figure 6-figure supplement 2VIIa) and found also here that G_{28} (tSbC) RGCs displayed the strongest tuning to ground-to-sky transitions among all dorsal RGCs (Figure 6-figure supplement 2VIIc-h, for statistics, see legends).

Visual context changes triggered by different behaviours, such as locomotion and head or eye movements will differ strongly with respect to their statistics – in particular with respect to their speed. Therefore, for G_{28} (tSbC) RGCs to play a role in detecting context changes, their detection performance should be robust across velocities. To test whether this is the case, we conducted additional *in-silico* experiments where we predicted responses of all RGC groups to stimuli simulating transitions across the visual field with and without context change (Figure 7h) at different velocities: 50, 150, 250, and 350 visual degrees per second (°/s; see Methods; Figure 6-figure supplement 3VIIIa,b) The slowest speed simulated visual input as could be elicited by locomotion, and the fastest speed approached that of saccades (48). We then performed an ROC analysis on the model cell responses, which confirmed that G_{28} RGCs could distinguish ground-to-sky context changes from all other types of transitions robustly across different speeds (Figure 7i,j). Interestingly, the advantage of G_{28} over other RGC groups in performing this detection task diminished with increasing speed (Figure 6-figure supplement 3VIIIc,d); see also Discussion).

Together, these analyses demonstrate that a downstream area, reading out from a single RGC group, would achieve the best performance in detecting ground-to-sky context changes if it based its decisions on inputs from G_{28} RGCs, robustly across different lighting conditions (transitions between movie snippets), retinal location (ventral and dorsal), and speeds. Since such an area would receive input not from a single cell, but from a local population of cells, the detection performance of single cells should represent a lower bound to that area's detection performance.

Discussion

We combined large-scale recordings of RGC responses to natural movie stimulation with CNN-based modelling to investigate colour processing in the mouse retina. By searching the stimulus space *in silico* to identify *most exciting inputs* (MEIs), we found a novel type of chromatic tuning in tSbC RGCs. We revealed this RGC type's pronounced and unique selectivity for full-field changes from green-dominated to UV-dominated scenes, a stimulus that matches the chromatic statistics of ground-to-sky transitions in natural scenes. Therefore, we suggest that tSbC cells may signal

context changes within their RF. Beyond our focus on tSbC cells, our study demonstrates the utility of an *in silico* approach for generating and testing hypotheses about the ethological relevance of sensory representations.

Nonlinear approaches for characterising neuronal selectivities and invariances. We leverage image-computable models in combination with an optimisation approach to search in dynamic, chromatic stimulus space for globally optimal inputs for RGCs, the MEIs. The resulting MEI represents the peak in the nonlinear loss landscape that describes the neuron's tuning in high-dimensional stimulus space. This approach has also been used to reveal the complexities and nonlinearities of neuronal tuning in monkey visual cortex area V4 (33, 42) and mouse area V1 (32, 34). Still, these approaches are not the "silver bullet" for identifying nonlinear selectivities. One important limitation is that searching for the *most* exciting input will return a single input – even when there are several inputs that would elicit equal response, such as ON and OFF stimuli for ON-OFF cells (see Figure II, G_{10} MEIs). A remedy for this limitation is to search for *diverse* exciting inputs by generating stimuli that are both highly effective at eliciting neural responses and at the same time distinct from one another. Ding et al. (49) used this approach to study bipartite invariance in mouse V1 (see also (50)). Related to this, Goldin et al. (51) searched for locally optimal stimulus perturbations for mouse RGCs and found that the selectivity for positive or negative contrast in a subset of cells is context-dependent. These cells signal absolute contrast, i.e. they are invariant to contrast polarity ("classical" ON vs. OFF). Together, these studies showcase the versatility of the toolkit of optimisation-based approaches at characterising nonlinear neuronal operations in high-dimensional, natural stimulus spaces. We add to this toolkit by first searching for a globally optimal stimulus, and then searching locally in its vicinity to map the cells' loss landscape around the maximum.

Circuit mechanisms for colour-opponency in tSbC RGCs. Most previous studies of colour-opponency in the mouse retina have identified sparse populations of colour-opponent RGCs that have not been systematically assigned to a particular functional type (20, 21, 52). The only studies that have examined the mechanisms of colour-opponency in identified mouse RGC types showed a centre-surround organisation, with RF centre and surround having different chromatic preferences ((18, 53); and (54), but see (55)). While we do not specifically analyse centre-surround opponency in this study, we see a similar trend as described previously in many RGC types, with stronger surrounds in the green channel relative to the UV channel (see Figure 4a, Figure 3-figure supplement 1II). tSbC RGCs, in contrast, respond to spatially co-extensive colour-opponent stimuli, functionally reminiscent of colour-opponent RGCs in Guinea pig (56) and ground squirrels (57).

In mice, centre-surround opponency has been attributed to the opsin gradient (53) and rod contributions in the outer retina (18, 20), whereas the circuitry for spatially co-extensive opponency remains unknown. It seems unlikely, though, that the opsin gradient plays a major role in the tSbC cell's colour opponency, because both ventral and dorsal tSbC cells preferentially responded to full-field green-to-UV transitions. In primates, spatially co-extensive colour-opponency in small bistratified RGCs is thought to arise from the selective wiring of S-ON and M/L-OFF bipolar cells onto the inner and outer dendritic strata, respectively ((58), but see (59)). A similar wiring pattern seems unlikely for tSbC RGCs, since their inner dendrites do not co-stratify with the S-ON (type 9) bipolar cells, nor do their outer dendrites co-stratify with the candidate M-OFF bipolar cell (type 1) (60). The bistratified dendritic arbour distinguishes the mouse tSbC also from the colour-opponent ON RGC type in Guinea pig, which is monostratified (56).

The large RF centres of the tSbC cells, extending well beyond their dendritic fields, come from a non-canonical circuit, in which tonic inhibition onto the RGC via $GABA_B$ receptors is relieved via serial inhibition from different amacrine cells using $GABA_C$ receptors (36). An intriguing possibility is that a colour-selective amacrine cell is part of this circuit, perhaps supporting chromatically tuned disinhibition in the absence of selective wiring from the aforementioned cone-selective bipolar cells onto the RGC.

A new functional role for tSbC RGCs. Suppressed-by-contrast responses have been recorded along the early visual pathway in dorsal lateral geniculate nucleus (dLGN), superior colliculus (SC), and primary visual cortex (V1) (61–63), with their function still being debated (64). In the retina, three types of SbC RGCs have so far been identified (reviewed in (45)), among them the tSbC cell (36–38). Despite their relatively recent discovery, tSbC RGCs have been suggested to play a role in several different visual computations. The first report of their light responses in mice connected them to the SbC RGCs previously discovered in rabbit, cat, and macaque, and suggested a role in signalling self-generated stimuli, perhaps for saccade suppression (37). Aided by a new intersectional transgenic line to selectively label tSbC RGCs (38), their projections were traced to areas in SC, v- and dLGN, and nucleus of the optic tract (NOT). The latter stabilises horizontal eye movements; however, as the medial terminal nucleus (MTN), which serves stabilisation of vertical eye movements, lacks tSbC innervation, it is unclear whether and how these RGCs contribute to gaze stabilisation.

A retinal study identified the circuit mechanisms responsible for some of the unique spatial and temporal response properties of tSbC cells and suggested a possible role in defocus detection to drive emmetropization in growing eyes and accommodation in adults (36, 65). Here, we identified another potential role for these RGCs in vision based on the chromatic properties of their RFs: signalling visual context changes (see next section). These different possible functional roles are not mutually exclusive, and might even be complementary in some cases, highlighting the difficulty in assigning single features to distinct RGC types (16). In

particular, the centre colour-opponency that we discovered in tSbC RGCs could serve to enhance their role in defocus detection by adding a directional signal (myopic vs. hyperopic) based on the chromatic aberration of lens and cornea (66). Future studies may test these theories by manipulating these cells *in vivo* using the new transgenic tSbC mouse line (38).

Behavioural relevance of context change detection. The horizon is a prominent landmark in visual space: it bisects the visual field into two regions, ground and sky. This is particularly relevant in animals like mice, where eye motion largely accounts for head movements and keeps the visual field stable with respect to the horizon (48). Visual stimuli carry different meaning depending on where they occur relative to the horizon, and context-specific processing of visual inputs is necessary for selecting appropriate behavioural responses (reviewed in (67)). For example, it is sensible to assume that a looming stimulus above the horizon is a predator, the appropriate response to which would be avoidance (that is, escape or freezing). A similar stimulus below the horizon, however, is more likely to be harmless or even prey. To allow for time-critical perceptual decisions – predator or prey – and corresponding behavioural response selection – avoidance or approach – it might be useful that stimulus (e.g., dark moving spot) and contextual information converge soon in the visual circuitry. Notably, VGluT3-expressing amacrine cells (a "hub" for distributing information about motion) represent a shared element in upstream circuitry, providing opposite-sign input to tSbC and to RGCs implicated in triggering avoidance behaviour, such as tOFF α (13, 46) and W3 cells (68). In downstream circuitry, SbC inputs have been found to converge with "conventional" RGC inputs onto targets in dLGN and NOT; whether tSbC axons specifically converge with tOFF α or W3 axons remains to be tested. Such convergence may allow "flagging" the activity of these RGCs with their local context (sky/threat or ground/no threat).

Depending on the behaviour that elicits a context change – be it a head or eye movement or locomotion – the parameters of the incoming stimulus, such as illumination level and velocity, may change. To be behaviourally useful, a context-change-flagging signal needs to be reliable and robust across these different stimulus parameters. While many slow-ON RGCs achieve high detection performance at higher transition velocities, probably reacting to the increasingly flash-like stimuli, tSbC RGCs were the only type with robustly high performance across different levels of illumination and all simulated speeds.

***In-silico* approaches to linking neural tuning and function.** The modelling of retinal responses to natural stimuli has advanced our understanding of the complexity of retinal processing in recent years. As suggested in a recent review, it is helpful to consider the contributions of different studies in terms of one of three perspectives on the retinal encoding of natural scenes: The circuit perspective ("how?"), the normative perspective ("why?"), and the coding perspective ("what?") (69). For example, an *in-silico* dissection of a CNN model of the retina offered explanations on how the surprisingly complex retinal computations, such as motion reversal, omitted stimulus response, and polarity reversal, emerge from simpler computations within retinal circuits (26, 27). Taking on the normative perspective, anatomically constrained deep CNNs trained on image recognition suggested a dependency between the complexity of retinal representations and the computational power of downstream cortical networks: Whereas a computationally powerful cortex, as found in primates, can deal with faithful, linear representations of visual inputs, a simpler cortical circuitry, as found in mice, requires more complex feature extraction upstream in the retina ((70, 71); but see (72)). However, the full potential of CNN models as tools for understanding sensory processing goes beyond response prediction and reproducing effects that are already described in the literature.

Here, we developed an approach that allows investigating the complexity of retinal processing simultaneously from the coding and the normative perspectives: A global search for most exciting mouse RGC inputs in dynamic, chromatic stimulus space answers the question of *what* it is that retinal neurons encode. Interpreting the abstract features extracted by the retina against the backdrop of natural stimulus space points to *why* these features might be behaviourally relevant. And finally, classifying individual RGCs into types then allows to bring in the circuit perspective through targeted experiments aimed at dissecting *how* specific retinal computations are implemented.

Methods

Animals and tissue preparation. All imaging experiments were conducted at the University of Tübingen; the corresponding animal procedures were approved by the governmental review board (Regierungspräsidium Tübingen, Baden-Württemberg, Konrad-Adenauer-Str. 20, 72072 Tübingen, Germany) and performed according to the laws governing animal experimentation issued by the German Government. All electrophysiological experiments were conducted at Northwestern University; the corresponding animal procedures were performed according to standards provided by Northwestern University Center for Comparative Medicine and approved by the Institutional Animal Care and Use Committee (IACUC).

For all imaging experiments, we used 4- to 15-week-old C57Bl/6 J mice (n=23; JAX 000664) of either sex (10 male, 13 female). These animals were housed under a standard 12 h day/night rhythm at 22° and 55% humidity. On the day of the recording experiment, animals were dark-adapted for at least 1 h, then anaesthetised with isoflurane (Baxter) and killed by cervical dislocation. All following procedures were carried out under very dim red (> 650 nm) light. The eyes were enucleated and hemisected in carboxygenated (95% O_2, 5% CO_2) artificial cerebrospinal fluid (ACSF) solution containing (in mM): 125 NaCl, 2.5 KCl, 2 $CaCl_2$, 1 $MgCl_2$, 1.25 NaH_2PO_4, 26 $NaHCO_3$, 20 glu-

cose, and 0.5 L-glutamine at pH 7.4. Next, the retinae were bulk-electroporated with the fluorescent Ca^{2+} indicator Oregon–Green BAPTA-1 (OGB-1), as described earlier (73). In brief, the dissected retina was flat-mounted onto an Anodisc (#13, 0.2 µm pore size, GE Healthcare) with the RGCs facing up, and placed between a pair of 4-mm horizontal plate electrodes (CUY700P4E/L, Nepagene/Xceltis). A 10-μl drop of 5 mM OGB-1 (hexapotassium salt; Life Technologies) in ACSF was suspended from the upper electrode and lowered onto the retina. Next, nine pulses ($\approx$9.2 V, 100 ms pulse width, at 1 Hz) from a pulse generator/wideband amplifier combination (TGP110 and WA301, Thurlby handar/Farnell) were applied. Finally, the tissue was placed into the microscope's recording chamber, where it was perfused with carboxygenated ACSF (at $\approx$36° C) and left to recover for $\geq$30 min before recordings started. To visualise vessels and damaged cells in the red fluorescence channel, the ACSF contained $\approx$0.1 μM Sulforhodamine-101 (SR101, Invitrogen) (74). All procedures were carried out under dim red (>650 nm) light.

For electrophysiology experiments, we used ChAT-Cre (JAX 006410) x Ai14 (JAX 007914) mice on a C57Bl/6J background (n=2, male, aged 27 and 30 weeks). Mice were housed with siblings in groups up to 4, fed normal mouse chow and maintained on a 12:12 h light/dark cycle. Before the experiment, mice were dark-adapted overnight and sacrificed by cervical dislocation. Retinal tissue was isolated under infrared illumination (900 nm) with the aid of night-vision goggles and IR dissection scope attachments (BE Meyers). Retinal orientation was identified using scleral landmarks (75), and preserved using relieving cuts in cardinal directions, with the largest cut at the dorsal retina. Retinas were mounted on 12mm poly-D-lysine coated glass affixed to a recording dish with grease, with the GCL up. Oxygenation was maintained by superfusing the dish with carboxygenated Ames medium (US Biological, A1372-25) warmed to 32 °C. For cell-attached single cell recordings, we used Symphony software (https://symphony-das.github.io/) with custom extensions (https://github.com/Schwartz-AlaLaurila-Labs/sa-labs-extension).

Owing to the exploratory nature of our study, we did not use randomisation and blinding. No statistical methods were used to predetermine sample size.

Two-photon calcium imaging. We used a MOM-type two-photon microscope (designed by W. Denk; purchased from Sutter Instruments) (74, 76), which was equipped with a mode-locked Ti:Sapphire laser (MaiTai-HP DeepSee, Newport Spectra-Physics) tuned to 927 nm, two fluorescence detection channels for OGB-1 (HQ 510/84, AHF/Chroma) and SR101 (HQ 630/60, AHF), and a water immersion objective (CF175 $LWD \times 16$/0.8W, DIC N2, Nikon, Germany). Image acquisition was performed with custom-made software (ScanM by M. Müller and T.E.) running under IGOR Pro 6.3 for Windows (Wavemetrics), taking time-lapsed 64×64 pixel image scans ($\approx (100\ \mu m)^2$ at 7.8125 Hz (Figure 1c). For simplicity, we refer to such a time-lapsed scan of a local population of GCL cells as a "recording". Despite the low frame rate, the Ca^{2+} responses can be related to the spike rate (77–80). For documenting the position of the recording fields, the retina under the microscope was oriented such that the most ventral edge pointed always towards the experimenter. In addition, higher resolution images (512×512 pixel) were acquired and recording field positions relative to the optic nerve were routinely logged.

Data preprocessing. Ca^{2+} traces were extracted for individual ROIs as described previously (6, 20). Extracted traces $\mathbf{c}_{raw}$ were then detrended to remove slow drifts in the recorded signal that were unrelated to changes in the neural response. First, a smoothed version of the traces, $\mathbf{c}_{smooth}$, was calculated by applying a Savitzky-Golay filter of 3rd polynomial order and a window length of 60 s using the SciPy implementation `scipy.signal.savgol_filter`. This smoothed version was then subtracted from the raw traces to yield the detrended traces.

$$\mathbf{c}_{detrend} = \mathbf{c}_{raw} - \mathbf{c}_{smooth}$$

To make traces non-negative ($\mathbf{c}_+$), we then clipped all values smaller than the 2.5^{th} percentile, $\eta_{2.5}$, to that value, and then subtracted $\eta_{2.5}$ from the detrended traces:

$$\mathbf{c}_+ = \mathbf{c}_{detrend} - \eta_{2.5}$$

This procedure (i.e. clipping to, and subtracting $\eta_{2.5}$) was more robust than simply subtracting the minimum.

Finally, traces were then divided by the standard deviation within the time window before stimulus start at t_0:

$$\mathbf{c} := \mathbf{c}_{final} = \frac{\mathbf{c}_{nn}}{SD(\mathbf{c}_{+[:t_0]})}$$

For training the model on movie response, we then estimated firing rates $\mathbf{r}$ from the detrended Ca^{2+} traces $\mathbf{c}$ using the package C2S (https://github.com/lucastheis/c2s, Theis et al. (80)).

Inclusion criteria. We applied a sequence of quality filtering steps to recorded cells before analysis illustrated in Figure 1-figure supplement 1Ic. As a first step, we applied a general response quality criterion, defined as a sufficiently reliable response to the Moving bar stimulus (as quantified by a quality index $QI_{MB} > 0.6$), *or* a sufficiently reliable response to the chirp stimulus (as quantified by a quality index $QI_{chirp} > 0.35$). The quality index is defined as in ref.(6):

$$QI = \frac{\mathrm{Var}[\langle \boldsymbol{r} \rangle_i]_t}{\langle \mathrm{Var}[\boldsymbol{r}]_t \rangle_i}$$

where $\boldsymbol{r}$ is the T by I response matrix (time samples by stimulus repetitions) and $\langle\rangle_x$ and $\mathrm{Var}[]_x$ denote the mean and variance across the indicated dimension x, respectively.

The second and third step made sure only cells were included that were assigned to a ganglion cell group (i.e., group index between 1 and 32) with sufficient confidence.

Confidence is defined as the probability assigned to the predicted class by the random forest classifier (see (81)), and the threshold was set at ≥ 0.25.

The fourth step made sure only cells with a sufficient model prediction performance, defined as an average single-trial test set correlation of $\langle C(\hat{r}^{(n)}, r_i^{(n)})\rangle_i > .3$, were included.

All cells passing steps 1-3 were included in the horizon detection analysis (Figure 7); all cells passing steps 1-4 were included in the MEI analysis (Figure 3); the "red" cells passing steps 1-4 were included in the MEI validation analysis (Figure 4). In the process of analysing MEIs, we fitted DoGs to their green and UV spatial component (see Methods section Concentric anisotropic 2D Difference-of-Gaussians fit). For the analysis of MEI properties (temporal frequency, centre size, chromatic contrast), we only included cells with a sufficient DoG goodness-of-fit, determined as a value of the cost function of $< .11$ for both green and UV on the resulting DoG fit. This threshold was determined by visual inspection of the DoG fits and led to the inclusion of 1613 out of 1947 RGCs in the MEI property analysis.

Visual stimulation. For light stimulation (imaging experiments), we projected the image generated by a digital light processing (DLP) projector (lightcrafter DPM-FE4500MKIIF, EKB Technologies Ltd) through the objective onto the tissue. The lightcrafter featured a light-guide port to couple in external, band-pass filtered UV and green LEDs (light-emitting diodes) (green: 576 BP 10, F37-576; UV: 387 BP 11, F39-387; both AHF/Chroma) (82). To optimise spectral separation of mouse M- and S-opsins, LEDs were band-pass filtered (390/576 dual-band, F59-003, AHF/Chroma). LEDs were synchronised with the microscope's scan retrace. Stimulator intensity (as photoisomerization rate, 10^3 P^*s^{-1} per cone) was calibrated to range from $\approx$0.5 (black image) to $\approx$20 for M- and S-opsins, respectively. Additionally, we estimated a steady illumination component of $\approx 10^4$ P^*s^{-1} per cone to be present during the recordings because of two photon excitation of photopigments (74, 76). Before data acquisition, the retina was adapted to the light stimulation by presenting a binary noise stimulus (20×15 matrix, $(40\,\mu\text{m})^2$ pixels, balanced random sequence) at 5 Hz for 5 min to the tissue.

For electrophysiology experiments, stimuli were presented using a digital projector (DPM-FE4500MKII, EKB Technologies Ltd) at a frame rate of 60 Hz and a spatial resolution of 1140 $\times$ 912 pixels (1.3 μm per pixel) focused on the photoreceptor layer. Neutral density filters (Thorlabs), a triple-band pass filter (405 BP 20, 485 BP 20, 552 BP 16; 69000x, Chroma), and a custom LED controller circuit were used to attenuate the light intensity of stimuli either to match that of the Ca^{2+} imaging experiments (for MEI presentation) or to range from $\approx$ 0-200 P^*s^{-1} per rod (for cell identification). Stimuli were presented using Symphony software (https://symphony-das.github.io/) with custom extensions (https://github.com/Schwartz-AlaLaurila-Labs/sa-labs-extension).

Identifying retinal ganglion cell types. To functionally identify RGC groups in the Ca^{2+} imaging experiments, we used our default "fingerprinting" stimuli, as described earlier (6). These stimuli included a full-field (700 μm in diameter) chirp stimulus, and a 300 $\times$ 1,000 μm bright bar moving at 1,000 $\mu\text{m}\cdot s^{-1}$ in eight directions across the recording field (with the shorter edge leading; Figure 1b).

The procedure and rationale for identifying cells in the electrophysiological recordings is presented in ref. (8). Cells with responses that qualitatively matched that of the OND and ON α types were included in the study. Following recording, cells were filled with AlexaFluor-488 by patch pipette and imaged under a two-photon microscope. Dendrites were traced in Fiji (NIH) using the SNT plugin (83). Dendritic arbours were computationally flattened using a custom MATLAB tool (https://doi.org/10.5281/zenodo.6578530) based on the method in ref. (84) to further confirm their identity as morphological type 73 from ref. (9).

Mouse natural movies. The natural movie stimulus consisted of clips of natural scenes recording outside in the field with a specialised, calibrated camera (5). This camera featured a fish-eye lens, and two spectral channels, UV (band-pass filter F37-424, AHF, $>$90% transmission at 350–419 nm) and green (F47-510, $>$90%, 470–550 nm, AHF), approximating the spectral sensitivities of mouse opsins (35). In mice, eye movements often serve to stabilise the image on the retina during head movements (48). Therefore, the camera was also stabilised by mounting it on a gimbal. As a result, the horizon bisected the camera's visual field.

A *mouse cam movie* frame contained a circular field of view (FOV) of 180° corresponding to 437 pixels along the diameter. To minimise the influence of potential chromatic and spatial aberrations introduced by the lenses, we focused on image cut-outs (crops; $30° \times 26°$, equivalent to 72×64 pixels in size) from upper and lower visual field, centred at $[28°, 56°]$ and $[-42°, -31°]$, respectively, relative to the horizon (for details, see (5)). Our *stimulus movie* consisted of 113 movie clips, each 150 frames (= 5 s) long. 108 clips were randomly reordered for each recording and split into two 54 clips-long *training sequences*. The remaining 5 clips formed a fixed *test sequence* that was presented before, in between, and after the training sequences (Figure 1b). To keep intensity changes at clip transitions small, we only used clips with mean intensities between 0.04 and 0.22 (for intensities in $[0, 1]$). For display during the experiments, intensities were then mapped to the range covered by the stimulator, i.e. $[0, 255]$.

Convolutional neural network model of the retina. We trained a convolutional neural network (CNN) model to predict responses of RGCs to a dichromatic natural movie. The CNN model consisted of two modules, a convolutional core that was shared between all neurons, and a readout that was specific for each neuron (85).

The core module was modelled as a two-layer convolutional neural network with 16 feature channels in each layer. Both layers consisted of space-time separable 3D convolutional kernels followed by a batch normalisation layer and an ELU (exponential linear unit) nonlinearity. In the first layer, sixteen $2 \times 11 \times 11 \times 21$ (c=#input channels (green and UV) $\times$ h=height $\times$ w=width $\times$ t=#frames) kernels were applied as valid convolution; in the second layer, sixteen $16 \times 5 \times 5 \times 11$ kernels were applied with zero padding along the spatial dimensions. We parameterised the temporal kernels as Fourier series and added one time stretching parameter per recording to account for inter-experimental variability affecting the speed of retinal processing. More precisely, every temporal kernel was represented by the first k sine and cosine functions, with trainable weights and phases, on an evenly spaced temporal grid, where $k = 7$ for the first layer, and $k = 3$ for the second layer. Additionally, we introduced a trainable stretch parameter for every recording to account for faster and slower response kernels. For example, the first layer temporal kernels are 21 steps long. Then, in order to stay well under the Nyquist limit, we parameterise the kernels with $k = 21/3 = 7$ sines and cosines.

For each of those sines and cosines a weight (α, β) is learned to represent the shape of the temporal responses kernel (shared among cells within a recording). Per scan i, the time grid t (21 steps from 0 to 1) is stretched by a factor τ_i to account for different response speeds. To avoid adding additional cycles (e.g., for stretch factors $\tau > 1$) this is masked by an exponential envelope

$$\epsilon(\tau) = \frac{1}{1 + \exp -(t + \frac{21 \cdot 0.95}{\tau})} \tag{1}$$

Thus,

$$w_i = \sum_j^k \alpha_j \sin(2\pi \cdot \tau_i \cdot t \cdot \epsilon(\tau_i)) + \beta_j \cos(2\pi \cdot \tau_i \cdot t \cdot \epsilon(\tau_i)). \tag{2}$$

is the temporal kernel parameterisation, that allows the model to learn a shared temporal filter that is made faster or slower for each specific scan (86).

In the readout, we modelled each cell's spatial receptive field (RF) as a 2D isotropic Gaussian, parameterised as $\mathcal{N}(\mu_x, \mu_y; \sigma)$. We then modelled the neural response as an affine function of the core feature maps weighted by the spatial RF, followed by a softplus nonlinearity.

For the linearised version of the model, the architecture was exactly the same except for the fact that there was no ELU nonlinearity after both convolutional layers. The resulting CNN was therefore equivalent to an LN model.

Model training and evaluation. We trained our network by minimising the Poisson loss

$$\sum_{n=1}^{N} \left(\hat{\boldsymbol{r}}^{(n)} - \boldsymbol{r}^{(n)} \log \hat{\boldsymbol{r}}^{(n)} \right)$$

where N is the number of neurons, $\boldsymbol{r}^{(n)}$ is the measured and $\hat{\boldsymbol{r}}^{(n)}$ the predicted firing rate of neuron n for an input of duration t=50 frames. We followed the training schedule of Lurz et al. (87). Specifically, we used early stopping (88) on the correlation between predicted and measured neuronal responses on the validation set, which consisted of 15 out of the 108 movie clips. If the correlation failed to increase during any 5 consecutive passes through the entire training set (epochs), we stopped the training and restored the model to the best performing model over the course of training. We went through 4 cycles of early stopping, restoring the model to the best performing, and continuing training, each time reducing the initial learning rate of 0.01 by a learning rate decay factor of 0.3. Network parameters were iteratively optimised via stochastic gradient descent using the Adam optimiser (89) with a batch size of 32 and a chunk size (number of frames for each element in the batch) of 50. For all analyses and MEI generation, we used an ensemble of models as described in ref. (34). Briefly, we trained 5 instances of the same model initialised with different random seeds. Inputs to the ensemble model were passed to each member and the final ensemble model prediction was obtained by averaging the outputs of the 5 members. For ease of notation, we thus redefine $\hat{\boldsymbol{r}}^{(n)}$ to be the *ensemble* model prediction.

After training, we evaluated model performance for each modelled neuron n as the correlation to the mean, i.e. the correlation between predicted response $\hat{r}^{(n)}$ and measured response $r^{(n)}$ to the held-out test sequence, the latter averaged across 3 repetitions $i = \{1, 2, 3\}$: $C(\hat{r}^{(n)}, \langle r_i^{(n)} \rangle_i)$. Unlike the single-trial correlation $C(\hat{r}^{(n)}, r_i^{(n)})$ which is always limited to values < 1 by inherent neuronal noise, a perfect model can in theory achieve a value of 1 for the correlation to the mean, in the limit of infinitely many repetitions when the sample average $\langle r^{(n)i} \rangle_i$ is a perfect estimate of the true underlying response $\rho^{(n)}$. The observed correlation to the mean can thus be interpreted as an estimate of the fraction of the maximally achievable correlation achieved by our model. For deciding which cells to exclude from analysis, we used average single-trial correlation $(\langle C(\hat{r}^{(n)}, r_i^{(n)}) \rangle_i)$ since this measure reflects both model performance as well as reliability of the neuronal response to the movie stimulus for neuron n (see also Methods section on Inclusion criteria).

Synthesising MEIs. We synthesised maximally exciting inputs for RGCs as described previously (32). Formally, for each model neuron n we wanted to find

$$\boldsymbol{x}^{*(n)} = \arg\max_{\boldsymbol{x}} \langle \hat{\boldsymbol{r}}^{(n)}(\boldsymbol{x})_{30:50} \rangle_t, \tag{3}$$

i.e. the input $\boldsymbol{x}^{*(n)}$ where the model neuron's response $\langle \hat{\boldsymbol{r}}(\boldsymbol{x})_{30:50} \rangle_t$, averaged across frames 30 to 50, attains a maximum, subject to norm and range constraints (see below). To this end, we randomly initialised an input $\boldsymbol{x}_0^{(n)} \in \mathcal{R}^{c \times w \times h \times t}$ of duration t=50 frames with Gaussian

white noise, and then iteratively updated $x_i^{(n)}$ according to the gradient of the model neuron's response:

$$\boldsymbol{x}_{i+1}^{(n)} = \boldsymbol{x}_i^{(n)} + \lambda \frac{\delta}{\delta \boldsymbol{x}_i^{(n)}} \langle \hat{\boldsymbol{r}}^{(n)}(\boldsymbol{x}_i^{(n)})_{30:50} \rangle_t, \qquad \textbf{(4)}$$

where $\lambda = 10$ was the learning rate. The optimisation was performed using Stochastic Gradient Descent (SGD), and was subject to a norm and a range constraint. The norm constraint was applied jointly across both channels and ensured that the L2 norm of each MEI did not exceed a fixed budget b of 30. The norm-constrained MEI $\tilde{\boldsymbol{x}}_i^{(n)}$ was calculated at each iteration as

$$\tilde{\boldsymbol{x}}_i^{(n)} = \frac{b}{||\boldsymbol{x}_i^{(n)}||_2} \times \boldsymbol{x}_i^{(n)} \qquad \textbf{(5)}$$

The range constraint was defined and applied for each colour channel separately and ensured that the range of the MEI values stayed within the range covered by the training movie. This was achieved by clipping values of the MEI exceeding the range covered by the training movie to the minimum or maximum value. Optimisation was run for at least 100 iterations, and then stopped when the number of iterations reached 1,000, or when it had converged (whichever occurred first). Convergence was defined as 10 consecutive iterations with a change in model neuron activation of less than 0.001; model neuron activations ranged from ≈ 1 to ≈ 10. We denote the resulting MEI for neuron n as $\boldsymbol{x}^{*(n)}$.

Analysing MEIs. We analysed MEIs to quantify their spatial, temporal, and chromatic properties.

Spatial and temporal components of MEIs. For each colour channel c, we decomposed the spatiotemporal MEIs into a spatial component and a temporal component by singular value decomposition:

$$U, S, V = \text{svd}(\boldsymbol{x}_c^{*(n)})$$

with $x_c^{*(n)} \in \mathcal{R}^{50\times288}$ for $c \in$ [green, UV] is the MEI of neuron n in a given colour channel with its spatial dimension ($18\times16 = 288$) flattened out. As a result, any spatiotemporal dependencies are removed and we only analyse spatial and temporal properties separately. The following procedures were carried out in the same manner for the green and the UV component of the MEI, and we drop the colour channel index c for ease of notation. The temporal component is then defined as the first left singular vector, $U_{:1}$, and the spatial component is defined as the first right singular vector, $V_{:1}^T$, reshaped to the original dimensions 18×16.

Concentric anisotropic 2D Difference-of-Gaussians fit. We modelled the spatial component as concentric anisotropic Difference-of-Gaussians (DoG) using the nonlinear least-squares solver `scipy.optimize.least_squares` with soft-L1 loss function (40). The DoGs were parameterized by a location (μ_x, μ_y) shared between centre and surround, amplitudes A^c, A^s, variances (σ_x^c, σ_y^c), (σ_x^s, σ_y^s), and rotation angles θ^c, θ^s separately for centre and surround:

$$\text{DoG} = G^c - G^s$$

with

$$G^c(x,y) = \mathrm{A}^c \exp(-f^c(x-\mu_x)^2 + 2g^c(y-\mu_y)(x-\mu_x) + h^c(y-\mu_y)^2)$$

and

$$f^c = \frac{\cos^2\theta^c}{2\sigma_x^c} + \frac{\sin^2\theta^c}{2\sigma_y^c},$$
$$g^c = \frac{\sin 2\theta^c}{4\sigma_y^c} - \frac{\sin 2\theta^c}{4\sigma_y^c},$$
$$h^c = \frac{\sin^2\theta^c}{2\sigma_x^c} + \frac{\cos^2\theta^c}{2\sigma_y^c},$$

and likewise for G^s. We initialised (μ_x, μ_y) in the following way: Since we set the model readout's location parameters to (0, 0) for all model neurons when generating their MEIs, we also expected the MEIs to be centred at (0, 0), as well. Hence, we determined the location of the minimum and the maximum value of the MEI; whichever was closer to the centre (0,0) provided the initial values for the parameters (μ_x, μ_y). Starting from there, we then first fit a single Gaussian to the MEI, and took the resulting parameters as initial parameters for the DoG fit. This was a constrained optimisation problem, with lower and upper bounds on all parameters; in particular, such that the location parameter would not exceed the canvas of the MEI, and such that the variance would be strictly positive.

MEI properties.

Centre size We defined the diameter of the centre of the MEI in the horizontal and the vertical orientation, respectively, as $d_x^c = 2\sigma_x^c$ and $d_y^c = 2\sigma_y^c$. The centre size was calculated as $\frac{1}{2}(d_x^c + d_y^c)$. We then estimated a contour outlining the MEI centre as the line that is defined by all points at which the 2D centre Gaussian G^c attains the value $G^c(x,y)$ with $(x,y) = (\mu_x + \sigma_x^c, \mu_y + \sigma_y^c)$. The centre mask m was then defined as a binary matrix with all pixels within the convex hull of this contour being 1 and all other pixels set to 0. This mask is used for calculating centre chromatic contrast (see below).

Temporal frequency To estimate temporal frequency of the MEIs, we estimated the power spectrum of the temporal components using a Fast Fourier Transform after attenuating high frequency noise by filtering with a 5$^{\text{th}}$ order low-pass

Butterworth filter with cutoff frequency 10 Hz. We then estimated the mean frequency of the temporal component by calculating an average of the frequency components, each weighted with its relative power.

Contrast The contrast of the MEIs in the two channels, $\gamma(\boldsymbol{x}_c^{*(n)})$ for $c \in$ [green, UV], was defined as the difference between the mean value within the centre mask m at the two last peaks of the temporal component of the MEI in the UV channel at time points t_2 and t_1:

$$\gamma(\boldsymbol{x}_c^{*(n)}) = (\boldsymbol{x}_c^{*(n)} \odot m)(t_2) - (\boldsymbol{x}_c^{*(n)} \odot m)(t_1),$$

where $\odot$ denotes the element-wise multiplication of the MEI and the binary mask. (see Figure 3f). The peaks were found with the function `scipy.signal.find_peaks`, and the peaks found for the UV channel were used to calculate contrast both in the green and the UV channel.

Validating MEIs experimentally.

Generating MEI stimuli. To test experimentally whether the model correctly predicts which stimuli would maximally excite RGCs of different RGC groups, we performed a new set of experiments (numbers indicated in red in Figure 1-figure supplement 1Ic), where we complemented our stimulus set with MEI stimuli. For the MEI stimuli, we selected 11 RGCs, chosen to span the responses space and to represent both well-described and poorly understood RGC groups, for which we generated MEIs at different positions on a 5×5 grid (spanning $110\mu m$ in vertical and horizontal direction). We decomposed the MEIs as described above, and reconstructed MEIs as rank 1 tensors by taking the outer product of the spatial and temporal components:

$$\bar{\boldsymbol{x}}^* = S_{11} U_{:1} \otimes V_{:1}^T$$

The MEI stimuli, lasting 50 frames (1.66 s) were padded with 10 frames (.34 s) of inter-stimulus grey, and were randomly interleaved. With 11 stimuli, presented at 25 positions and lasting 2 s each, the total stimulus duration was $11 \times 25 \times 2\ s = 550\ s$. Since the model operated on a z-scored (0 mean, 1 SD) version of the movie, MEIs as predicted by the model lived in the same space and had to be transformed back to the stimulator range ([0, 255]) before being used as stimuli in an experiment by scaling with the movie's SD and adding the movie's mean. The MEIs' green channel was then displayed with the green LED, and the UV channel was displayed with the UV LED. For experiments at Northwestern University, an additional transform was necessary to achieve the same levels of photoreceptor activation (photoisomerization rates) for M- and S-cones with different LEDs. To ensure proper chromatic scaling between the different experimental apparatuses with different spectral profiles, we described the relative activation of M- and S-cones by the green and UV LEDs in the stimulation setup used in the two photon imaging experiments (setup A) by a matrix

$$\mathbf{A} = \begin{bmatrix} a_{mg} & a_{sg} \\ a_{mu} & a_{su} \end{bmatrix} = \begin{bmatrix} 1 & 0.19 \\ 0 & 1 \end{bmatrix},$$

and the relative activation of M- and S-cones by the stimulation setup used in the patch-clamp experiments (setup B) by a matrix

$$\mathbf{B} = \begin{bmatrix} b_{mg} & b_{sg} \\ b_{mu} & b_{su} \end{bmatrix} = \begin{bmatrix} 1 & 0.9 \\ 0.035 & 1 \end{bmatrix},$$

where diagonal entries describe the activation of M-cones by the green LED, and of S-cones by the UV LED, and entries in the off-diagonal describe the cross-activation (i.e., M-cones by UV-LED and S-cones by green LED). The activation of M-cones and S-cones $\mathbf{e}^\mathbf{T} = (e_m, e_s)$ by a stimulus $\boldsymbol{x} \in \mathcal{R}^{2\times 1}$ displayed on a given stimulation setup was approximated as $\mathbf{e} = \mathbf{A}\boldsymbol{x}$ (90). Hence, a stimulus $\boldsymbol{x}'$ displayed on setup B, defined as $\boldsymbol{x}' = \mathbf{B}^{-1}\mathbf{A}\boldsymbol{x}$, will achieve the same photoreceptor activation as stimulus $\boldsymbol{x}$ displayed on setup A. Since the solution exceeded the valid range of the stimulator ([0, 255]), we added an offset and multiplied with a scalar factor to ensure all stimuli were within the valid range.

Analysing RGC responses to MEI stimuli. We wanted to evaluate the responses of RGCs to the MEI stimuli in a spatially resolved fashion, i.e. weighting responses to MEIs displayed at different locations proportional to the strength of the RGCs RF at that location. In order to be able to meaningfully compare MEI responses between RGCs and across groups, for each RGC, we first centred and scaled the responses to zero mean and a standard deviation of 1. Then, for each RGC n, we computed a spatial average of its responses, weighting its responses at each spatial location (x, y) proportional to the Gaussian density $\mathcal{N}_{\boldsymbol{\mu_n},\sigma_n}(x, y)$, where the parameters of the Gaussian $\boldsymbol{\mu_n} = (\mu_x, \mu_y), \sigma_n$ were the model's estimated readout parameters for neuron n (Figure 4b,c,d left):

$$\langle \boldsymbol{r}^{(n)} \rangle_{x,y} = \sum_{x'=1}^{5} \sum_{y'=1}^{5} \boldsymbol{r}^{(n)}_{x',y'} \cdot \mathcal{N}_{\boldsymbol{\mu_n},\sigma_n}(x', y')$$

where $\boldsymbol{r}^{(n)}_{x',y'} \in \mathcal{R}^{11\times 60}$ is the 60 frames (2 s) long response of neuron n to an MEI at position $(x, y) = (x', y')$, resampled from the recording frame rate of 7.81 Hz to 30 Hz. We then averaged $\langle \boldsymbol{r}^{(i)} \rangle_{x,y}$ across time in the optimisation time window, i.e. frames 30-50, to get a scalar response $\tilde{r}^{(n)} = \langle \boldsymbol{r}^{(n)} \rangle_{x,y,t}$ for each MEI stimulus (Figure 4d).

Selectivity index. To quantify the selectivity of the response $\tilde{r}^{(n)}(\boldsymbol{x_i^*})$ of an RGC n to an MEI $\boldsymbol{x_i^*}$, we defined a selectivity index as follows. First, we standardised the responses $\tilde{r}^{(n)}$ across all MEIs by subtracting the mean and dividing by the standard deviation. The selectivity index of RGC group $\mathrm{G_g}$ to MEI $\boldsymbol{x_i^*}$ was then defined as

$$\mathrm{SI}_g(\boldsymbol{x_i^*}) = \langle \tilde{r}^{(n)}(\boldsymbol{x_i^*}) - \frac{1}{10}\sum_{j=1}^{11} \delta_{ij}\tilde{r}^{(n)}(\boldsymbol{x_j^*})\rangle_n,$$

where δ_{ij} is the Kronecker delta. In words, the SI is the difference (in units of SD response) between the response to the MEI of interest ($\boldsymbol{x_i^*}$) and the mean response to all other (10) MEIs, $\frac{1}{10}\sum_{j=1}^{11}\delta_{ij}\tilde{r}^{(n)}(\boldsymbol{x_j^*})$, averaged across all cells n belonging to the group of interest $\mathrm{G_g}$.

Characterising nonlinear processing of chromatic contrast space. We wanted to analyse the tuning of $\mathrm{G_{28}}$/tSbC RGCs to chromatic contrast and to this end, we mapped the model response and its gradient across chromatic contrast space (Figure 6). Specifically, the MEIs have $d = 2 \times 18 \times 16 \times 50 = 28,800$ pixels and dimensions, $14,400$ for each colour channel. Now let $x^{*(n)} \in \mathcal{R}^{1x28800}$ be the cell's MEI estimated using the LN model, with the first d=14,400 dimensions defining the green pixels and the remaining dimensions defining the UV pixels. Then for each cell we consider a two-dimensional subspace spanned by two basis vectors $\mathbf{e}_1, \mathbf{e}_2$ where

$$\mathbf{e}_1 = \begin{bmatrix} x_1^{*(n)} \\ x_2^{*(n)} \\ \vdots \\ x_d^{*(n)} \\ 0 \\ \vdots \\ 0 \end{bmatrix} \quad \mathbf{e}_2 = \begin{bmatrix} 0 \\ \vdots \\ 0 \\ x_1^{*(n)} \\ x_2^{*(n)} \\ \vdots \\ x_d^{*(n)} \end{bmatrix}$$

In words, the basis vectors consist of the UV component of the MEI in the UV channel and 0s in the green channel for $\mathbf{e}_1$, and of 0s in the UV channel and the UV component of the MEI in the green channel for $\mathbf{e}_2$. We chose this subspace due to its vicinity to the optimum of the neuron's tuning curve, and we chose the UV MEI as component of both basis vectors, since the green and UV component of $\mathrm{G_{28}}$ MEIs were very similar except for their temporal contrast (see Figure 3-figure supplement 1II). We then sampled 11 points along each dimension, equally spaced between $[-1, 1]$, which resulted in stimuli that are identical in terms of their spatial and temporal properties and only differ in their contrast. We then evaluated the model neuron response at these points in the subspace (Figure 6d). We also evaluated the gradient of the model neuron response at these points and plotted the direction of the gradient projected into the subspace spanned by e_1, e_2 (Figure 6b,c).

Detection performance analysis. To test the performance of individual RGCs of different groups in detecting the target class of inter-clip transitions (ground-to-sky) from all other classes of inter-clip transitions, we performed a receiver operating characteristic (ROC) analysis (47). For each RGC, we calculated its response to an inter-clip transition occurring at time t_0 as the baseline-subtracted average response within 1 second following the transition, i.e. $\frac{1}{T}\sum_{t=0}^{T} r(t) - r(t_0)$, with T=30 frames at 30 Hz. For all n=40 equally spaced thresholds within the response range of a RGC, we then calculated the true positive rate (TPR) and false positive rate (FPR) of a hypothetical classifier classifying all transitions eliciting an above-threshold response as a positive, and all other transitions as negative. Plotting the TPR as a function of FPR yields an ROC curve, the area under which (AUC) is equivalent to the probability that the RGC will respond more strongly to a randomly chosen inter-clip transition of the target class than to a randomly chosen inter-clip transition of a different class. The AUC thus is a measure of performance for RGCs in this detection task.

Detection task in simulation. We simulated the four types of transitions (sky-sky, sky-ground, ground-ground, ground-sky) in natural scenes to include various visual context changes across velocities, which could be triggered by different behaviours such as locomotion or eye movements. With the simulated context-changing stimuli, we predicted model neuron responses *in-silico* and then determined if $\mathrm{G_{28}}$ could perform the detection task robustly well across speeds.

For generating the stimuli, 500 frames were randomly extracted from the same mouse natural movies used for the 2P-imaging experiments. For each frame, we simulated visual transitions by moving a 72 x 64 pixel-large window along a fixed trajectory (Figure 7h bottom) at four different angular velocities: 50, 150, 250, and 350°/s, corresponding to 4, 12, 20, and 28 pixels per frame, respectively (Figure 6-figure supplement 3VIIIa,b). Each edge of the trajectory is 220 pixels long, covering 90.6°of visual angle. Each selected scene frame was sampled 8 times (that is, twice per velocity). To avoid potential biases due to asymmetries in the mouse natural movie, we sampled each frame for each velocity both in clockwise and counterclockwise direction. The stimuli were then down-sampled to 18 x 14 pixels and shown to the model at a frame rate of 30 Hz. Because the trajectories contained different numbers of moving frames for the 4 velocities, we "padded" the stimuli at the beginning and the end of each transition stimulus by duplicating the start and end frames, resulting in a total of 60 frames each (see illustration in Figure 6-figure supplement 3VIIIb).

Statistical analysis.

Permutation test. We wanted to test how likely the difference in AUC observed for different RGC groups are to occur under the null hypothesis that the underlying distributions they are sampled from are equal. To this end, we performed a permutation test. We generated a null distribution for our test statistic, the absolute difference in AUC values ΔAUC, by shuffling the RGC group labels of the two groups of interest (e.g. $\mathrm{G_{28}}$ and $\mathrm{G_{24}}$) and calculating the test statistic with shuffled labels 100,000 times. We only included RGC groups with at least N=4 cells in this analysis. We then obtained a p-value for ΔAUC observed with true labels as the proportion of entries in the null distribution larger than ΔAUC.

Bootstrapped confidence intervals. We bootstrapped confidence intervals for ΔAUC (Figure 7 and Figure 6-figure supplement 2VII). For ΔAUC, we generated a bootstrapped distribution by sampling 100 times with replacement from the AUC values of the two groups that were being compared and calculated ΔAUC. We then estimated the 95 % confidence interval for ΔAUC as the interval defined by the 2.5^{th} and 97.5^{th} percentile of the bootstrapped distribution of ΔAUC.

For $\Gamma(\phi_s, \phi_{\nu_g})$, we generated a bootstrapped distribution by sampling 100 times with replacement from the MEI responses of RGC group g and then calculating $\text{RDM}^{\phi_{\nu_g}}$ and $\Gamma(\phi_s, \phi_{\nu_g})$ for each sample. We then estimated the 95 % confidence interval for $\Gamma(\phi_s, \phi_{\nu_g})$ as the interval defined by the 2.5^{th} and 97.5^{th} percentile of the bootstrapped distribution of $\Gamma(\phi_s, \phi_{\nu_g})$.

Estimating effect size. The effect size of difference in AUC observed for different RGC groups l and k, ΔAUC (Figure 7 and Figure 6-figure supplement 2VII), was estimated as Cohen's d (91, 92):

$$\frac{|m_k - m_l|}{s},$$

with

$$s = \sqrt{\frac{(N_k - 1)s_k^2 + (N_l - 1)s_l^2}{N_k + N_l - 2}}$$

and m_k and s_k the sample mean and standard deviation, respectively, of the AUC observed for the N_k RGCs of group k.

Estimating linear correlation. Wherever the linear correlation between two paired samples x and y of size N was calculated (for evaluating model performance, Figure 2, Figure 1-figure supplement 1I, Figure 4-figure supplement 1IV, we used Pearson's correlation coefficient:

$$C_{xy} = \frac{\sum_i^N (x_i - \bar{x})(y_i - \bar{y})}{\sqrt{\sum_i^N (x_i - \bar{x})^2}\sqrt{\sum_i^N (y_i - \bar{y})^2}}$$

Data availability

The data and the movie stimulus will be made available at https://retinal-functomics.net upon journal publication.

Code availability

Custom analysis and model training code will be made available at https://github.com/eulerlab upon journal publication.

Author contributions

L. H.: Conceptualisation, methodology, software, validation, formal analysis, data curation, writing (original draft), visualisation **K. P. S.**: validation, investigation, data curation **C. B.**: methodology, software, formal analysis **Y. D.**: methodology, validation, visualisation, writing (review and editing) **Y. Q.**: resources, software **D. A. K.**: methodology, software, writing (review and editing) **Z. J.**: methodology, validation, investigation, visualisation, writing (original draft) **G. W. S.**: methodology, validation, investigation, writing (original draft), supervision, funding acquisition **M. B.**: conceptualisation, writing (review and editing), supervision, funding acquisition **P. B.**: conceptualisation, writing (review and editing), supervision, funding acquisition **K. F.**: conceptualisation, writing (review and editing), supervision, funding acquisition **A. S. E.**: conceptualisation, writing (review and editing), supervision, funding acquisition **T. E.**: conceptualisation, writing (original draft), visualisation, supervision, funding acquisition, project administration.

ACKNOWLEDGEMENTS

We thank Jonathan Oesterle and Dominic Gonschorek for feedback on the manuscript, Jan Lause for statistical consulting, and Merle Harrer for general assistance. We also thank all members of the Sinz lab for regular discussions on the project. This work was supported by the German Research Foundation (DFG; CRC 1233 "Robust Vision: Inference Principles and Neural Mechanisms", project number 276693517 to P.B., M.B., T.E., K.F.; Heisenberg Professorship, BE5601/8-1 to P.B.; Excellence Cluster EXC 2064, project number 390727645 to P.B.; CRC 1456 "Mathematics of Experiment" project number 432680300 to A.S.E.), the Federal Ministry of Education and Research (FKZ 01IS18039A to P.B.), National Institutes of Health (NIH; NEI EY031029, NEI EY031329 to G.W.S.; NEI F30EY031565, NIGMS T32GM008152 to Z.J.), and the European Research Council (ERC) under the European Union's Horizon Europe research and innovation programme (A.S.E., grant agreement No. 101041669).

Bibliography

1. J Y Lettvin, H R Maturana, W S McCulloch, and W H Pitts. What the Frog's Eye Tells the Frog's Brain. *Proceedings of the IRE*, 47(11):1940–1959, 1959.
2. Tom Baden, Thomas Euler, and Philipp Berens. Understanding the retinal basis of vision across species. *Nature Reviews Neuroscience*, 21(1):5–20, 2020. ISSN 14710048. doi: 10.1038/s41583-019-0242-1.
3. Maxwell H. Turner, Luis Gonzalo Sanchez Giraldo, Odelia Schwartz, and Fred Rieke. Stimulus- and goal-oriented frameworks for understanding natural vision. *Nature Neuroscience*, 22(1):15–24, 2019. ISSN 15461726. doi: 10.1038/s41593-018-0284-0.
4. Eero P Simoncelli and Bruno A Olshausen. Natural Image Statistics and Neural Representation. *Annual Reviews Neurosciences*, 24:1193–1216, 2001.
5. Yongrong Qiu, Zhijian Zhao, David Klindt, Magdalena Kautzky, Klaudia P. Szatko, Frank Schaeffel, Katharina Rifai, Katrin Franke, Laura Busse, and Thomas Euler. Natural environment statistics in the upper and lower visual field are reflected in mouse retinal specializations. *Current Biology*, 31(15):3233–3247, 2021. ISSN 18790445. doi: 10.1016/j.cub.2021.05.017.
6. Tom Baden, Philipp Berens, Katrin Franke, Miroslav Román Rosón, Matthias Bethge, and Thomas Euler. The functional diversity of retinal ganglion cells in the mouse. *Nature*, 529 (7586):345–350, 2016. ISSN 15206041. doi: 10.1038/nature16468.
7. Daniel Kerschensteiner. Feature Detection by Retinal Ganglion Cells. *Annual Review of Vision Science*, 8(1):1–35, 9 2022. ISSN 2374-4642. doi: 10.1146/annurev-vision-100419-112009.
8. Jillian Goetz, Zachary F. Jessen, Anne Jacobi, Adam Mani, Sam Cooler, Devon Greer, Sabah Kadri, Jeremy Segal, Karthik Shekhar, Joshua R. Sanes, and Gregory W. Schwartz. Unified classification of mouse retinal ganglion cells using function, morphology, and gene expression. *Cell Reports*, 40(2):111040, 7 2022. ISSN 22111247. doi: 10.1016/j.celrep.2022.111040.
9. J. Alexander Bae, Shang Mu, Jinseop S. Kim, Nicholas L. Turner, Ignacio Tartavull, Nico Kemnitz, Chris S. Jordan, Alex D. Norton, William M. Silversmith, Rachel Prentki, Marissa Sorek, Celia David, Devon L. Jones, Doug Bland, Amy L.R. Sterling, Jungman Park, Kevin L. Briggman, and H. Sebastian Seung. Digital Museum of Retinal Ganglion Cells with Dense Anatomy and Physiology. *Cell*, 173(5):1293–1306, 2018. ISSN 10974172. doi: 10.1016/j.cell.2018.04.040.
10. Bruce A. Rheaume, Amyeo Jereen, Mohan Bolisetty, Muhammad S. Sajid, Yue Yang, Kathleen Renna, Lili Sun, Paul Robson, and Ephraim F. Trakhtenberg. Single cell transcriptome profiling of retinal ganglion cells identifies cellular subtypes. *Nature Communications*, 9(1), 2018. ISSN 20411723. doi: 10.1038/s41467-018-05134-3.
11. Emily M. Martersteck, Karla E. Hirokawa, Mariah Evarts, Amy Bernard, Xin Duan, Yang Li, Lydia Ng, Seung W. Oh, Benjamin Ouellette, Joshua J. Royall, Michelle Stoecklin, Quanxin Wang, Hongkui Zeng, Joshua R. Sanes, and Julie A. Harris. Diverse Central Projection Patterns of Retinal Ganglion Cells. *Cell Reports*, 18(8):2058–2072, 2 2017. ISSN 22111247. doi: 10.1016/j.celrep.2017.01.075.

12. Keith P Johnson, Michael J Fitzpatrick, Lei Zhao, Bing Wang, Sean McCracken, Philip R Williams, and Daniel Kerschensteiner. Cell-type-specific binocular vision guides predation in mice. *Neuron*, 3 2021. ISSN 0896-6273. doi: 10.1016/j.neuron.2021.03.010.
13. Thomas A. Münch, Rava Azeredo Da Silveira, Sandra Siegert, Tim James Viney, Gautam B. Awatramani, and Botond Roska. Approach sensitivity in the retina processed by a multifunctional neural circuit. *Nature Neuroscience*, 12(10):1308–1316, 2009. ISSN 10976256. doi: 10.1038/nn.2389.
14. Melis Yilmaz and Markus Meister. Rapid innate defensive responses of mice to looming visual stimuli. *Current Biology*, 23(20):2011–2015, 2013. ISSN 09609822. doi: 10.1016/j.cub.2013.08.015.
15. T. Kim, N. Shen, J. C. Hsiang, K. P. Johnson, and D. Kerschensteiner. Dendritic and parallel processing of visual threats in the retina control defensive responses. *Science Advances*, 6(47):1–12, 2020. ISSN 23752548. doi: 10.1126/sciadv.abc9920.
16. Gregory W. Schwartz and David Swygart. Circuits for Feature Selectivity in the Inner Retina. In *The Senses: A Comprehensive Reference*, pages 275–292. Elsevier, 1 2020. doi: 10.1016/b978-0-12-809324-5.24186-2.
17. A. Szél, P. Röhlich, A. R. Caffé, B. Juliusson, G. Aguirre, and T. Van Veen. Unique topographic separation of two spectral classes of cones in the mouse retina. *Journal of Comparative Neurology*, 325(3):327–342, 1992. ISSN 0021-9967. doi: 10.1002/cne.903250302.
18. Maximilian Joesch and Markus Meister. A neuronal circuit for colour vision based on rod-cone opponency. *Nature*, 532(7598):236–239, 2016. ISSN 14764687. doi: 10.1038/nature17158.
19. Tom Baden, Timm Schubert, Le Chang, Tao Wei, Mariana Zaichuk, Bernd Wissinger, and Thomas Euler. A tale of two retinal domains: Near-Optimal sampling of achromatic contrasts in natural scenes through asymmetric photoreceptor distribution. *Neuron*, 80(5):1206–1217, 2013. ISSN 08966273. doi: 10.1016/j.neuron.2013.09.030.
20. Klaudia P. Szatko, Maria M. Korympidou, Yanli Ran, Philipp Berens, Deniz Dalkara, Timm Schubert, Thomas Euler, and Katrin Franke. Neural circuits in the mouse retina support color vision in the upper visual field. *Nature Communications*, 11(1), 2020. ISSN 20411723. doi: 10.1038/s41467-020-17113-8.
21. Mohammad Hossein Khani and Tim Gollisch. Linear and nonlinear chromatic integration in the mouse retina. *Nature Communications*, 12(1):1900, 12 2021. ISSN 2041-1723. doi: 10.1038/s41467-021-22042-1.
22. Josh W. Mouland, Abigail Pienaar, Christopher Williams, Alex J. Watson, Robert J. Lucas, and Timothy M. Brown. Extensive cone-dependent spectral opponency within a discrete zone of the lateral geniculate nucleus supporting mouse color vision. *Current Biology*, 31(15):3391–3400, 2021. ISSN 18790445. doi: 10.1016/j.cub.2021.05.024.
23. Dimokratis Karamanlis and Tim Gollisch. Nonlinear spatial integration underlies the diversity of retinal ganglion cell responses to natural images. *Journal of Neuroscience*, 41(15):3479–3498, 4 2021. ISSN 15292401. doi: 10.1523/JNEUROSCI.3075-20.2021.
24. Tatyana O. Sharpee. Computational identification of receptive fields. *Annual Review of Neuroscience*, 36:103–120, 2013. ISSN 0147006X. doi: 10.1146/annurev-neuro-062012-170253.
25. Lane T. McIntosh, Niru Maheswaranathan, Aran Nayebi, Surya Ganguli, and Stephen A. Baccus. Deep Learning Models of the Retinal Response to Natural Scenes. *Neural Information Processing Systems (NIPS)*, (Nips):1–9, 2016. ISSN 1053-2498. doi: 10.1172/JCI44752.288.
26. Niru Maheswaranathan, Lane T. McIntosh, Hidenori Tanaka, Satchel Grant, David B Kastner, Joshua B Melander, Aran Nayebi, Luke E Brezovec, Julia H Wang, Surya Ganguli, and Stephen A Baccus. Interpreting the retinal neural code for natural scenes: From computations to neurons. *Neuron*, 111(17):2742–2755, 2023. ISSN 10974199. doi: 10.1016/j.neuron.2023.06.007.
27. Hidenori Tanaka, Aran Nayebi, Niru Maheswaranathan, Lane T. McIntosh, Stephen A. Baccus, and Surya Ganguli. From deep learning to mechanistic understanding in neuroscience: the structure of retinal prediction. *Proceedings of the 33rd Conference on Neural Information Processing Systems (NeurIPS 2019)*, (33):1–11, 2019.
28. Eleanor Batty, Josh Merel, Nora Brackbill, Alexander Heitman, Alexander Sher, Alan Litke, E. J. Chichilnisky, and Liam Paninski. Multilayer Recurrent Network Models of Primate Retinal Ganglion Cell Responses. *Proceedings of the 5th International Conference on Learning Representations*, (5), 2017.
29. Daniel L.K. Yamins, Ha Hong, Charles F Cadieu, Ethan A Solomon, Darren Seibert, and James J. DiCarlo. Performance-optimized hierarchical models predict neural responses in higher visual cortex. *Proceedings of the National Academy of Sciences of the United States of America*, 111(23):8619–8624, 2014. ISSN 10916490. doi: 10.1073/pnas.1403112111.
30. Santiago A Cadena, George H Denfield, Edgar Y Walker, Leon A Gatys, Andreas S Tolias, Matthias Bethge, and Alexander S Ecker. Deep convolutional models improve predictions of macaque V1 responses to natural images. *PLoS Computational Biology*, 15(4):1–28, 2019. ISSN 15537358. doi: 10.1371/journal.pcbi.1006897.
31. Ivan Ustyuzhaninov, Max F Burg, Santiago A Cadena, Jiakun Fu, Taliah Muhammad, Kayla Ponder, Emmanouil Froudarakis, Zhiwei Ding, Matthias Bethge, Andreas S Tolias, and Alexander S Ecker. Digital twin reveals combinatorial code of non-linear computations in the mouse primary visual cortex. *bioRxiv*, page 2022.02.10.479884, 2 2022. doi: 10.1101/2022.02.10.479884.
32. Edgar Y. Walker, Fabian H. Sinz, Erick Cobos, Taliah Muhammad, Emmanouil Froudarakis, Paul G. Fahey, Alexander S. Ecker, Jacob Reimer, Xaq Pitkow, and Andreas S. Tolias. Inception loops discover what excites neurons most using deep predictive models. *Nature Neuroscience*, 22(December), 2019. ISSN 15461726. doi: 10.1038/s41593-019-0517-x.
33. Pouya Bashivan, Kohitij Kar, and James J. DiCarlo. Neural population control via deep image synthesis. *Science*, 364(6439), 2019. ISSN 10959203. doi: 10.1126/science.aav9436.
34. Katrin Franke, Konstantin F Willeke, Kayla Ponder, Mario Galdamez, Na Zhou, Taliah Muhammad, Saumil Patel, Emmanouil Froudarakis, Jacob Reimer, Fabian H Sinz, and Andreas S Tolias. State-dependent pupil dilation rapidly shifts visual feature selectivity. *Nature*, 9 2022. ISSN 0028-0836. doi: 10.1038/s41586-022-05270-3.
35. Gerald H. Jacobs, Gary A. Williams, and John A. Fenwick. Influence of cone pigment coexpression on spectral sensitivity and color vision in the mouse. *Vision Research*, 44(14):1615–1622, 2004. ISSN 00426989. doi: 10.1016/j.visres.2004.01.016.
36. Adam Mani and Gregory W. Schwartz. Circuit Mechanisms of a Retinal Ganglion Cell with Stimulus-Dependent Response Latency and Activation Beyond Its Dendrites. *Current Biology*, 27(4):471–482, 2017. ISSN 09609822. doi: 10.1016/j.cub.2016.12.033.
37. Nai Wen Tien, James T. Pearson, Charles R. Heller, Jay Demas, and Daniel Kerschensteiner. Genetically identified suppressed-by-contrast retinal ganglion cells reliably signal self-generated visual stimuli. *Journal of Neuroscience*, 35(30):10815–10820, 2015. ISSN 15292401. doi: 10.1523/JNEUROSCI.1521-15.2015.
38. Nai-Wen Tien, Carmela Vitale, Tudor C. Badea, and Daniel Kerschensteiner. Layer-Specific Developmentally Precise Axon Targeting of Transient Suppressed-by-Contrast Retinal Ganglion Cells (tSbC RGCs). *The Journal of Neuroscience*, 42(38):2332–21, 9 2022. ISSN 0270-6474. doi: 10.1523/jneurosci.2332-21.2022.
39. Luca Abballe and Hiroki Asari. Natural image statistics for mouse vision. *PloS ONE*, 17(1):e0262763, 2022. doi: 10.1371/journal.pone.0262763.
40. Divyansh Gupta, Wiktor Mlynarski, Olga Symonova, Jan Svaton, and Maximilian Joesch. Panoramic visual statistics shape retina-wide organization of receptive fields. *bioRxiv*, pages 1–31, 2022.
41. E J Chichilnisky. A simple white noise analysis of neuronal light responses. *Network: Computation in Neural Systems*, 12(2):199–213, 2001. ISSN 0954-898X. doi: 10.1080/713663221.
42. Konstantin F Willeke, Kelli Restivo, Katrin Franke, Arne F Nix, Santiago A Cadena, Tori Shinn, Cate Nealley, Gabrielle Rodriguez, Saumil Patel, Alexander S Ecker, Fabian H Sinz, and Andreas S Tolias. Deep learning-driven characterization of single cell tuning in primate visual area V4 unveils topological organization. *bioRxiv*, 5 2023. doi: 10.1101/2023.05.12.540591.
43. Gregory William Schwartz. Chapter 16 - Color processing. In Gregory William Schwartz, editor, *Retinal Computation*, pages 288–317. Academic Press, 2021. ISBN 978-0-12-819896-4. doi: https://doi.org/10.1016/B978-0-12-819896-4.00017-2.
44. Nai Wen Tien, Tahnbee Kim, and Daniel Kerschensteiner. Target-Specific Glycinergic Transmission from VGluT3-Expressing Amacrine Cells Shapes Suppressive Contrast Responses in the Retina. *Cell Reports*, 15(7):1369–1375, 5 2016. ISSN 22111247. doi: 10.1016/j.celrep.2016.04.025.
45. Jason Jacoby and Gregory William Schwartz. Typology and Circuitry of Suppressed-by-Contrast Retinal Ganglion Cells. *Frontiers in Cellular Neuroscience*, 12(August):1–7, 2018. ISSN 16625102. doi: 10.3389/fncel.2018.00269.
46. Brenna Krieger, Mu Qiao, David L. Rousso, Joshua R. Sanes, and Markus Meister. Four alpha ganglion cell types in mouse retina: Function, structure, and molecular signatures. *PLoS ONE*, 12(7):1–21, 2017. ISSN 19326203. doi: 10.1371/journal.pone.0180091.
47. Tom Fawcett. An introduction to ROC analysis. *Pattern Recognition Letters*, 27(8):861–874, 6 2006. ISSN 01678655. doi: 10.1016/j.patrec.2005.10.010.
48. Arne F. Meyer, John O'Keefe, and Jasper Poort. Two Distinct Types of Eye-Head Coupling in Freely Moving Mice. *Current Biology*, 30(11):2116–2130, 2020. ISSN 18790445. doi: 10.1016/j.cub.2020.04.042.
49. Zhiwei Ding, Dat T Tran, Kayla Ponder, Erick Cobos, Zhuokun Ding, Paul G Fahey, Eric Wang, Taliah Muhammad, Jiakun Fu, Santiago A Cadena, Stelios Papadopoulos, Saumil Patel, Katrin Franke, Jacob Reimer, Fabian H Sinz, Alexander S Ecker, Xaq Pitkow, and Andreas S Tolias. Bipartite invariance in mouse primary visual cortex. *bioRxiv*, 2023. doi: 10.1101/2023.03.15.532836.
50. Santiago A Cadena, Marissa A Weis, Leon A Gatys, Matthias Bethge, and Alexander S Ecker. Diverse Feature Visualizations Reveal Invariances in Early Layers of Deep Neural Networks. In *Computer Vision - ECCV 2018*, pages 225–240. 2018. ISBN 9783030012571. doi: 10.1007/978-3-030-01258-8{_}14.
51. Matías A Goldin, Baptiste Lefebvre, Samuele Virgili, Mathieu Kim Pham Van Cang, Alexander Ecker, Thierry Mora, Ulisse Ferrari, and Olivier Marre. Context-dependent selectivity to natural images in the retina. *Nature Communications*, 13(1), 2022. ISSN 20411723. doi: 10.1038/s41467-022-33242-8.
52. Peter Gouras and Bjorn Eskesen. Why do mice have ultra-violet vision? *Experimental Eye Research*, 79(6):887–892, 12 2004. ISSN 00144835. doi: 10.1016/j.exer.2004.06.031.
53. Le Chang, Tobias Breuninger, and Thomas Euler. Chromatic Coding from Cone-type Unselective Circuits in the Mouse Retina. *Neuron*, 77(3):559–571, 2013. ISSN 08966273. doi: 10.1016/j.neuron.2012.12.012.
54. Maureen E. Stabio, Shai Sabbah, Lauren E. Quattrochi, Marissa C. Ilardi, P. Michelle Fogerson, Megan L. Leyrer, Min Tae Kim, Inkyu Kim, Matthew Schiel, Jordan M. Renna, Kevin L. Briggman, and David M. Berson. The M5 Cell: A Color-Opponent Intrinsically Photosensitive Retinal Ganglion Cell. *Neuron*, 97(1):150–163, 2018. ISSN 10974199. doi: 10.1016/j.neuron.2017.11.030.
55. Takuma Sonoda, Yudai Okabe, and Tiffany M. Schmidt. Overlapping morphological and functional properties between M4 and M5 intrinsically photosensitive retinal ganglion cells. *Journal of Comparative Neurology*, 528(6):1028–1040, 4 2020. ISSN 10969861. doi: 10.1002/cne.24806.
56. Lu Yin, Robert G. Smith, Peter Sterling, and David H. Brainard. Physiology and morphology of color-opponent ganglion cells in a retina expressing a dual gradient of S and M opsins. *Journal of Neuroscience*, 29(9):2706–2724, 3 2009. ISSN 02706474. doi: 10.1523/JNEUROSCI.5471-08.2009.
57. C. R. Michael. Receptive fields of single optic nerve fibers in a mammal with an all-cone retina. I: contrast-sensitive units. *Journal of neurophysiology*, 31(2):249–256, 1968. ISSN 00223077. doi: 10.1152/jn.1968.31.2.249.
58. Dennis M. Dacey and Barry B. Lee. The 'blue-on' opponent pathway in primate retina originates from a distinct bistratified ganglion cell type. *Nature*, 367(6465):731–735, 1994. ISSN 00280836. doi: 10.1038/367731a0.
59. Greg D. Field, Alexander Sher, Jeffrey L. Gauthier, Martin Greschner, Jonathon Shlens, Alan M. Litke, and E. J. Chichilnisky. Spatial properties and functional organization of small bistratified ganglion cells in primate retina. *Journal of Neuroscience*, 27(48):13261–13272, 11 2007. ISSN 02706474. doi: 10.1523/JNEUROSCI.3437-07.2007.

60. Christian Behrens, Timm Schubert, Silke Haverkamp, Thomas Euler, and Philipp Berens. Connectivity map of bipolar cells and photoreceptors in the mouse retina. *eLife*, 5 (NOVEMBER2016):1–20, 2016. ISSN 2050084X. doi: 10.7554/eLife.20041.
61. Cristopher M. Niell and Michael P. Stryker. Modulation of Visual Responses by Behavioral State in Mouse Visual Cortex. *Neuron*, 65(4):472–479, 2010. ISSN 08966273. doi: 10.1016/j.neuron.2010.01.033.
62. Denise M. Piscopo, Rana N. El-Danaf, Andrew D. Huberman, and Cristopher M. Niell. Diverse visual features encoded in mouse lateral geniculate nucleus. *Journal of Neuroscience*, 33(11):4642–4656, 3 2013. ISSN 02706474. doi: 10.1523/JNEUROSCI.5187-12.2013.
63. Shinya Ito, David A. Feldheim, and Alan M. Litke. Segregation of visual response properties in the mouse superior colliculus and their modulation during locomotion. *Journal of Neuroscience*, 37(35):8428–8443, 8 2017. ISSN 15292401. doi: 10.1523/JNEUROSCI.3689-16.2017.
64. Richard H. Masland and Paul R. Martin. The unsolved mystery of vision. *Current Biology*, 17(15):R577–R582, 8 2007. ISSN 09609822. doi: 10.1016/j.cub.2007.05.040.
65. Tom Baden, Frank Schaeffel, and Philipp Berens. Visual Neuroscience: A Retinal Ganglion Cell to Report Image Focus? *Current Biology*, 27(4):R139–R141, 2 2017. ISSN 09609822. doi: 10.1016/j.cub.2016.12.022.
66. Timothy J. Gawne and Thomas T. Norton. An opponent dual-detector spectral drive model of emmetropization. *Vision Research*, 173:7–20, 8 2020. ISSN 18785646. doi: 10.1016/j.visres.2020.03.011.
67. Dominic A. Evans, A. Vanessa Stempel, Ruben Vale, and Tiago Branco. Cognitive Control of Escape Behaviour. *Trends in Cognitive Sciences*, 23(4):334–348, 4 2019. ISSN 1879307X. doi: 10.1016/j.tics.2019.01.012.
68. Y. Zhang, I.-J. Kim, J. R. Sanes, and M. Meister. The most numerous ganglion cell type of the mouse retina is a selective feature detector. *Proceedings of the National Academy of Sciences*, 109(36), 2012. ISSN 0027-8424. doi: 10.1073/pnas.1211547109.
69. Dimokratis Karamanlis, Helene Marianne Schreyer, and Tim Gollisch. Retinal Encoding of Natural Scenes. *Annual Review of Vision Science*, 8(1), 9 2022. ISSN 2374-4642. doi: 10.1146/annurev-vision-100820-114239.
70. Samuel A. Ocko, Jack Lindsey, Surya Ganguli, and Stephane Deny. The emergence of multiple retinal cell types through efficient coding of natural movies. *bioRxiv*, (NeurIPS): 458737, 2018. doi: 10.1101/458737.
71. Jack Lindsey, Samuel A. Ocko, Surya Ganguli, and Stephane Deny. A Unified Theory of Early Visual Representations from Retina to Cortex through Anatomically Constrained Deep CNNs. *International Conference on Learning Representations*, pages 1–17, 2019.
72. Tim Gollisch and Markus Meister. Eye Smarter than Scientists Believed: Neural Computations in Circuits of the Retina. *Neuron*, 65(2):150–164, 2010. ISSN 08966273. doi: 10.1016/j.neuron.2009.12.009.
73. Kevin L. Briggman and Thomas Euler. Bulk electroporation and population calcium imaging in the adult mammalian retina. *Journal of Neurophysiology*, 105(5):2601–2609, 2011. ISSN 00223077. doi: 10.1152/jn.00722.2010.
74. Thomas Euler, Susanne E Hausselt, David J Margolis, Tobias Breuninger, Xavier Castell, Peter B Detwiler, and Winfried Denk. Eyecup scope-optical recordings of light stimulus-evoked fluorescence signals in the retina. *Pflugers Archiv European Journal of Physiology*, 457(6):1393–1414, 2009. ISSN 00316768. doi: 10.1007/s00424-008-0603-5.
75. Wei Wei, Justin Elstrott, and Marla B. Feller. Two-photon targeted recording of GFP-expressing neurons for light responses and live-cell imaging in the mouse retina. *Nature Protocols*, 5(7):1347–1352, 7 2010. ISSN 17502799. doi: 10.1038/nprot.2010.106.
76. Thomas Euler, Katrin Franke, and Tom Baden. Studying a Light Sensor with Light: Multiphoton Imaging in the Retina. In Espen Hartveit, editor, *Multiphoton Microscopy*, chapter 10, pages 225–250. Humana Press, 2019. ISBN 9781493997015. doi: 10.1002/9781118696736.ch22.
77. Francesco Trapani, Giulia Spampinato, Pierre Yger, and Olivier Marre. Differences in nonlinearities determine retinal cell types. *Journal of Neurophysiology*, 130(3), 2023. doi: 10.1152/jn.00243.2022.
78. Miroslav Román Rosón, Yannik Bauer, Ann H. Kotkat, Philipp Berens, Thomas Euler, and Laura Busse. Mouse dLGN Receives Functional Input from a Diverse Population of Retinal Ganglion Cells with Limited Convergence. *Neuron*, 102(2):462–476, 2019. ISSN 10974199. doi: 10.1016/j.neuron.2019.01.040.
79. Philipp Berens, Jeremy Freeman, Thomas Deneux, Nicolay Chenkov, Thomas McColgan, Artur Speiser, Jakob H. Macke, Srinivas C. Turaga, Patrick Mineault, Peter Rupprecht, Stephan Gerhard, Rainer W. Friedrich, Johannes Friedrich, Liam Paninski, Marius Pachitariu, Kenneth D. Harris, Ben Bolte, Timothy A. Machado, Dario Ringach, Jasmine Stone, Luke E. Rogerson, Nicolas J. Sofroniew, Jacob Reimer, Emmanouil Froudarakis, Thomas Euler, Miroslav Román Rosón, Lucas Theis, Andreas S. Tolias, and Matthias Bethge. Community-based benchmarking improves spike rate inference from two-photon calcium imaging data. *PLoS Computational Biology*, 14(5):1–13, 2018. ISSN 15537358. doi: 10.1371/journal.pcbi.1006157.
80. Lucas Theis, Philipp Berens, Emmanouil Froudarakis, Jacob Reimer, Miroslav Román Rosón, Tom Baden, Thomas Euler, Andreas S. Tolias, and Matthias Bethge. Benchmarking Spike Rate Inference in Population Calcium Imaging. *Neuron*, 90(3):471–482, 2016. ISSN 10974199. doi: 10.1016/j.neuron.2016.04.014.
81. Yongrong Qiu, David A. Klindt, Klaudia P. Szatko, Dominic Gonschorek, Larissa Hoefling, Timm Schubert, Laura Busse, Matthias Bethge, and Thomas Euler. Efficient coding of natural scenes improves neural system identification. *PLOS Computational Biology*, 19 (4):e1011037, 4 2023. ISSN 1553-7358. doi: 10.1371/journal.pcbi.1011037.
82. Katrin Franke, André Maia Chagas, Zhijian Zhao, Maxime J.Y. Zimmermann, Philipp Bartel, Yongrong Qiu, Klaudia P. Szatko, Tom Baden, and Thomas Euler. An arbitrary-spectrum spatial visual stimulator for vision research. *eLife*, 8, 9 2019. ISSN 2050084X. doi: 10.7554/eLife.48779.
83. Cameron Arshadi, Ulrik Günther, Mark Eddison, Kyle I.S. Harrington, and Tiago A. Ferreira. SNT: a unifying toolbox for quantification of neuronal anatomy. *Nature Methods*, 18 (4):374–377, 4 2021. ISSN 15487105. doi: 10.1038/s41592-021-01105-7.
84. Uygar Sümbül, Sen Song, Kyle McCulloch, Michael Becker, Bin Lin, Joshua R. Sanes, Richard H. Masland, and H. Sebastian Seung. A genetic and computational approach to structurally classify neuronal types. *Nature Communications*, 5, 2014. ISSN 20411723. doi: 10.1038/ncomms4512.
85. David A. Klindt, Alexander S. Ecker, Thomas Euler, and Matthias Bethge. Neural system identification for large populations separating "what" and "where". *31st Conference on Neural Information Processing Systems*, (Nips):4–6, 2017. ISSN 10495258.
86. Zhijian Zhao, David A. Klindt, André Maia Chagas, Klaudia P. Szatko, Luke Rogerson, Dario A. Protti, Christian Behrens, Deniz Dalkara, Timm Schubert, Matthias Bethge, Katrin Franke, Philipp Berens, Alexander S. Ecker, and Thomas Euler. The temporal structure of the inner retina at a single glance. *Scientific Reports*, 10(1):4399, 12 2020. ISSN 2045-2322. doi: 10.1038/s41598-020-60214-z.
87. Konstantin-Klemens Lurz, Mohammad Bashiri, Konstantin Willeke, Akshay K Jagadish, Eric Wang, Edgar Y Walker, Santiago A Cadena, Taliah Muhammad, Erick Cobos, Andreas S Tolias, Alexander S Ecker, and Fabian H Sinz. Generalization in data-driven models of primary visual cortex. *Proceedings of the 9th International Conference on Learning Representations*, (9), 2021.
88. Lutz Prechelt. Early stopping - But when? In *Neural Networks:Tricks of the Trade. Lecture Notes in Computer Science*, volume 1524, pages 55–69. 1998. ISBN 9783642352881. doi: 10.1007/978-3-642-35289-8{_}5.
89. Diederik P. Kingma and Jimmy Ba. Adam: A Method for Stochastic Optimization. *Proceedings of the 3rd International Conference on Learning Representations*, (3):1–15, 2015. ISSN 09252312. doi: http://doi.acm.org.ezproxy.lib.ucf.edu/10.1145/1830483.1830503.
90. Matthias P. Christenson, S. Navid Mousavi, Elie Oriol, Sarah L. Heath, and Rudy Behnia. Exploiting colour space geometry for visual stimulus design across animals. *Philosophical Transactions of the Royal Society B: Biological Sciences*, 377(1862), 10 2022. ISSN 14712970. doi: 10.1098/rstb.2021.0280.
91. Jacob Cohen. *Statistical Power Analysis for the Behavioral Sciences*. Routledge, 5 1988. doi: 10.4324/9780203771587.
92. Jean-Christophe Goulet-Pelletier and Denis Cousineau. A review of effect sizes and their confidence intervals, Part I: The Cohen's d family. *The Quantitative Methods for Psychology*, 14(4):242–265, 12 2018. ISSN 2292-1354. doi: 10.20982/tqmp.14.4.p242.

Supplementary information

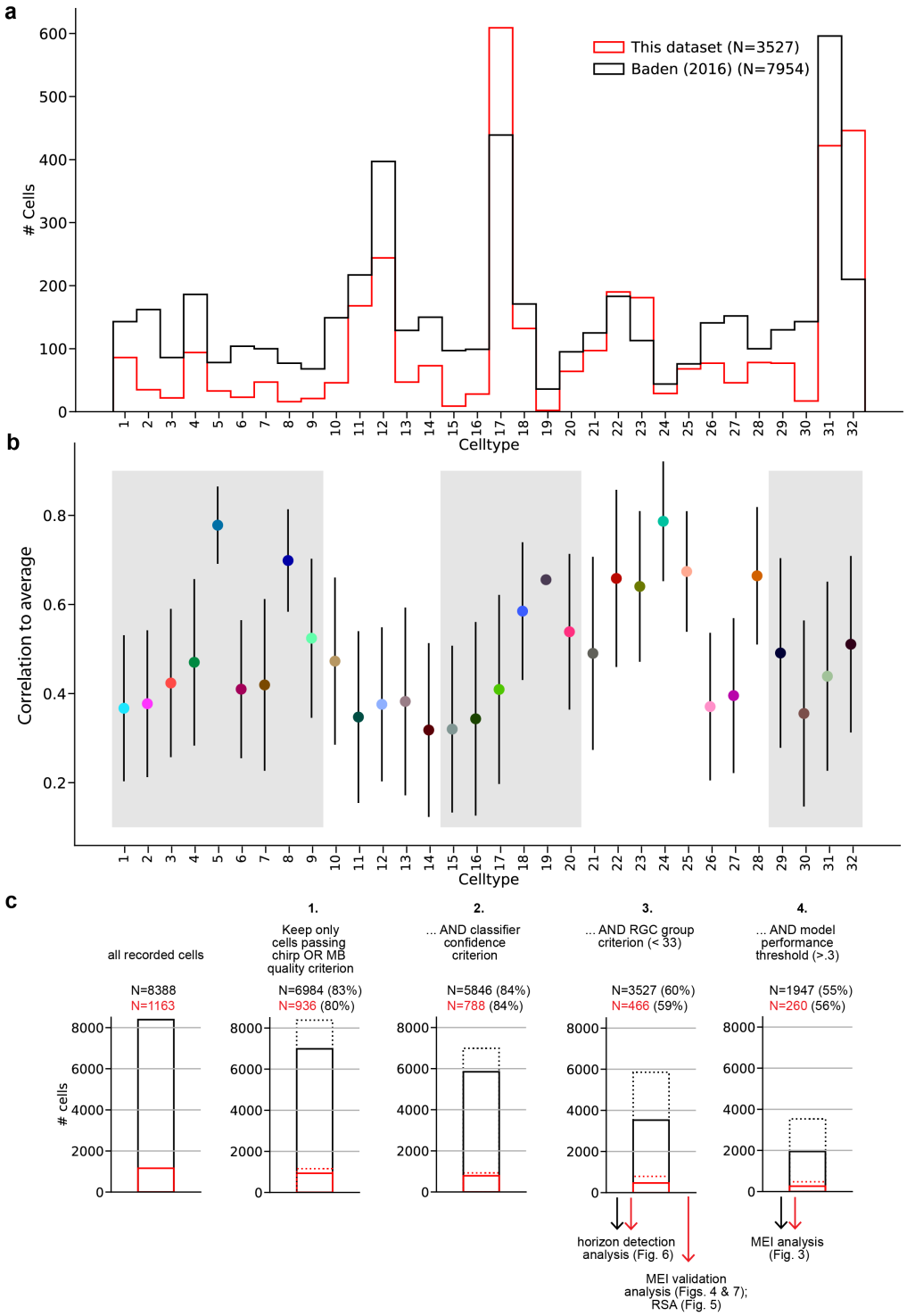

Figure I 1-figure supplement 1. (a) Distribution across cell types for this dataset, and for the dataset described in Baden et al. (6) which was the basis for our classifier (81). **(b)** Mean $\pm$ SD of model performance, evaluated as correlation between model prediction and RGC response on the 25 s long test sequence, averaged across 3 repetitions of the test sequence, for each cell type. **(c)** Response quality, RGC group assignment and model performance filtering pipeline showing the consecutive steps and the fraction of cells remaining after each step. Black bars and numbers indicate cells from all experiments (i.e. all RGCs for which we recorded chirp, MB, and movie responses), red bars and numbers indicate the subset of cells recorded in the MEI validation experiments (i.e. those RGCs for which we *additionally* recorded MEI stimuli responses). Dotted bars indicate the number of cells before the current filtering step. The filtering steps were as follows: **1.** Keep only cells that pass the chirp OR MB quality criterion ($\mathrm{QI}_{MB} > .6$ OR $\mathrm{QI}_{chirp} > .35$). **2.** Keep only cells that the classifier assigns to a group with confidence $\geq .25$. **3.** Keep only cells assigned to a ganglion cell group (groups 1-32; groups 33-46 are amacrine cell groups); **4.** Keep only cells with sufficiently high model performance ($\langle C(\hat{r}^{(n)}, r_i^{(n)}) \rangle_i > .3$). All cells passing steps 1-3 were included in the horizon detection analysis (Figure 7); all cells passing steps 1-4 were included in the MEI analysis (Figure 3); the "red" cells passing steps 1-4 were included in the MEI validation analysis (Figure 4). All quality criteria are described in the Methods section.

Figure II 3-figure supplement 1. Example MEIs for example cell types. Rows in each panel as in Figure 4a.

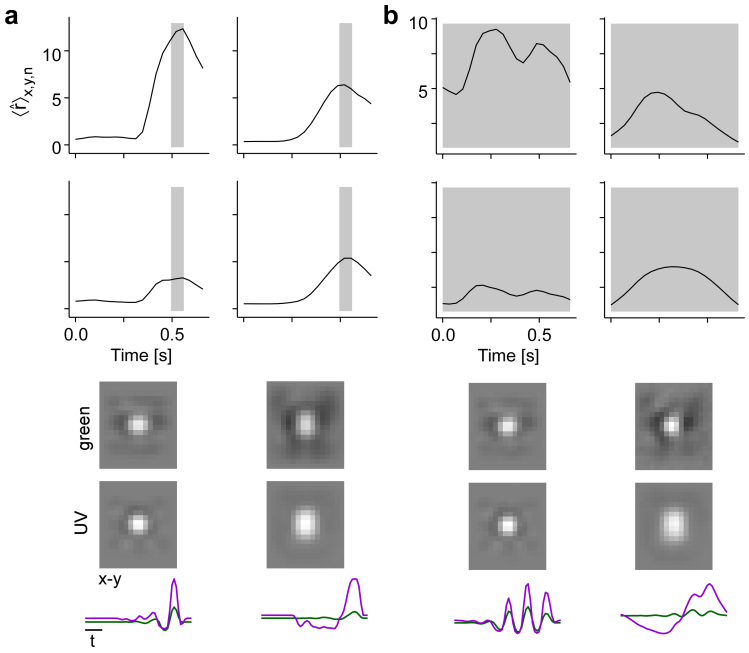

Figure III 3-figure supplement 2. Illustration of how different time windows for optimisation affect MEI temporal properties. **(a)** MEIs (bottom panels) and model neuron responses (top panels) for a short optimisation window of 2 frames ($\approx .066\ s$, indicated by grey shaded area). The top row shows the responses of a more transient RGC to its own MEI (left stimulus) and to the MEI of a more sustained RGC (right stimulus). The bottom row shows the responses of the more sustained RGC to its own MEI (right stimulus) and to the MEI of the more transient RGC (right stimulus). **(b)** MEIs (bottom panels) and model neuron responses (top panels) for a longer optimisation window of 20 frames ($\approx .66\ s$, indicated by grey shaded area) as used throughout the paper. The top row shows the responses of a more transient RGC to its own MEI (left stimulus) and to the MEI of a more sustained RGC (right stimulus). The bottom row shows the responses of the more sustained RGC to its own MEI (right stimulus) and to the MEI of the more transient RGC (right stimulus). Same cells as in (a).

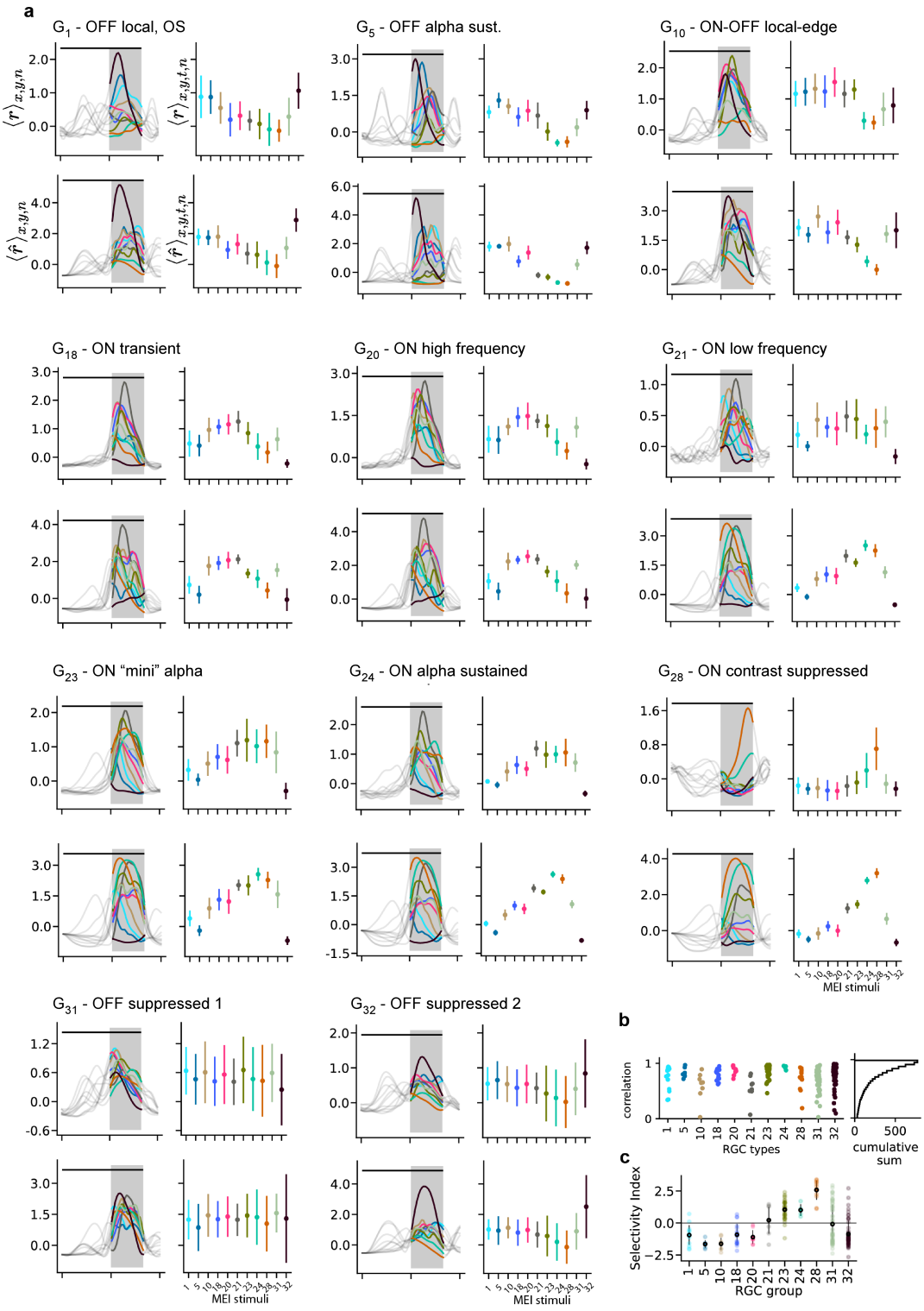

Figure IV 4-figure supplement 1. (a) Recorded (top, r) and predicted (bottom, $\hat{r}$) responses to the 11 different MEIs for all example cell types. Left: responses are averaged across the indicated dimensions x, y, n: different MEI locations (x, y) and RGCs in a group (n); black bar indicates stimulus duration (from 0 to 1.66 s), grey rectangle marks optimisation time window (from 1 to 1.66 s). Right: Responses to different MEIs, additionally averaged across time (t) within the optimisation time window. Error bars indicated SD across cells. **(b)** Correlation between the measured and predicted response magnitudes to the MEI stimuli per example cell type. Cumulative histogram is across all N=788 cells; 50% of cells have a correlation between measured and predicted response magnitude of ≥ 0.8. **(c)** Mean $\pm$ SD of selectivity index (see Methods) for the example cell groups, indicating the difference in response to MEI 28 vs. the average response to all other MEIs in units of standard deviation of the response.

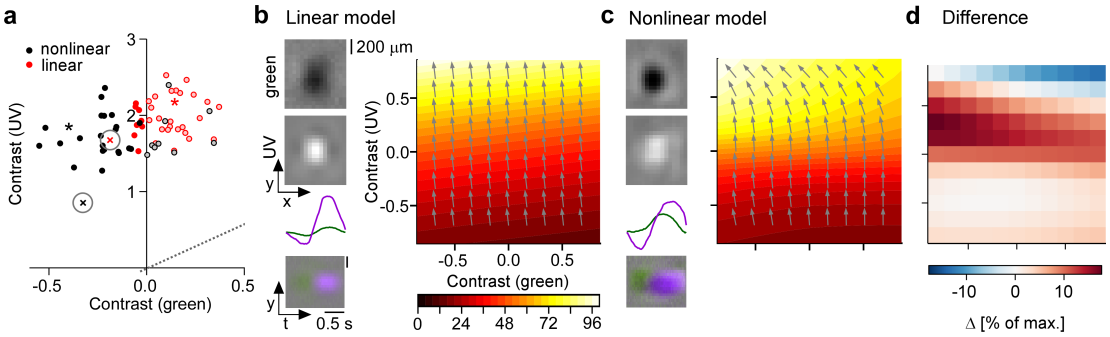

Figure V 5-figure supplement 1. (a) Distribution of green and UV MEI centre contrast for a linear-nonlinear (LN) model (red) and a CNN model (black); from Figure 6a. **(b,c)** Left: MEIs for a second example cell of RGC group G_{28}, generated with the LN model (b) or the CNN model (c). The cell's MEI centre contrast for both models is marked in (a) by cross. Right: Respective tuning maps of example neuron in chromatic contrast space. Colours represent responses in % of maximum response; arrows indicate the direction of the gradient across chromatic contrast space. **(d)** Difference in response between LN and CNN model (in % of maximum response).

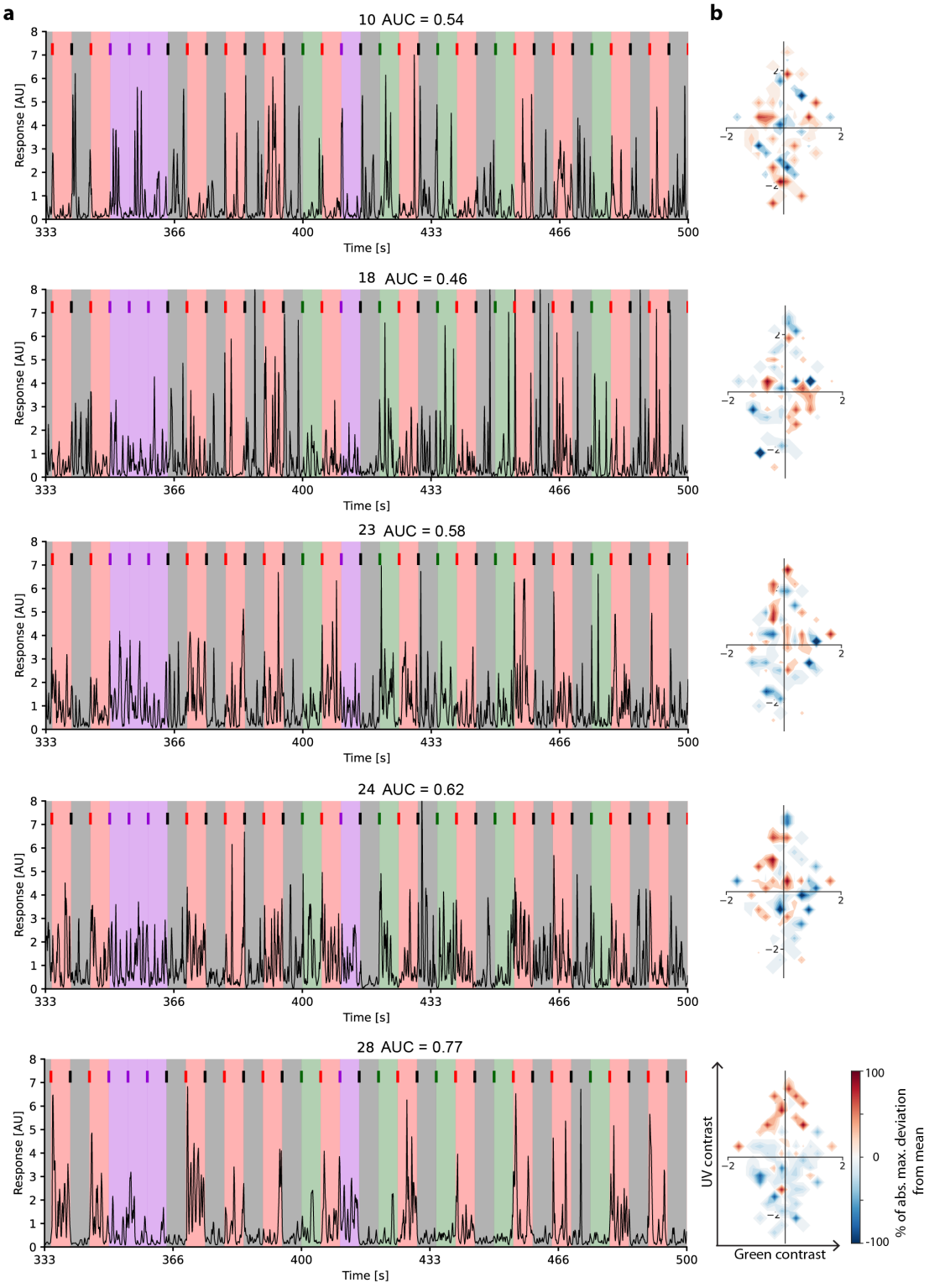

Figure VI 6-figure supplement 1. **(a)** Traces of example cells of different cell groups (G_{10}, G_{18}, G_{23}, G_{24}, G_{28}) from a single recording field, responding to 33 (of 122) inter-clip transitions. Inter-clip transitions are colour-coded by transition type (red: ground-to-sky, purple: sky-to-sky, green: ground-to-ground, black: sky-to-ground. **(b)** The resulting tuning maps in chromatic contrast space.

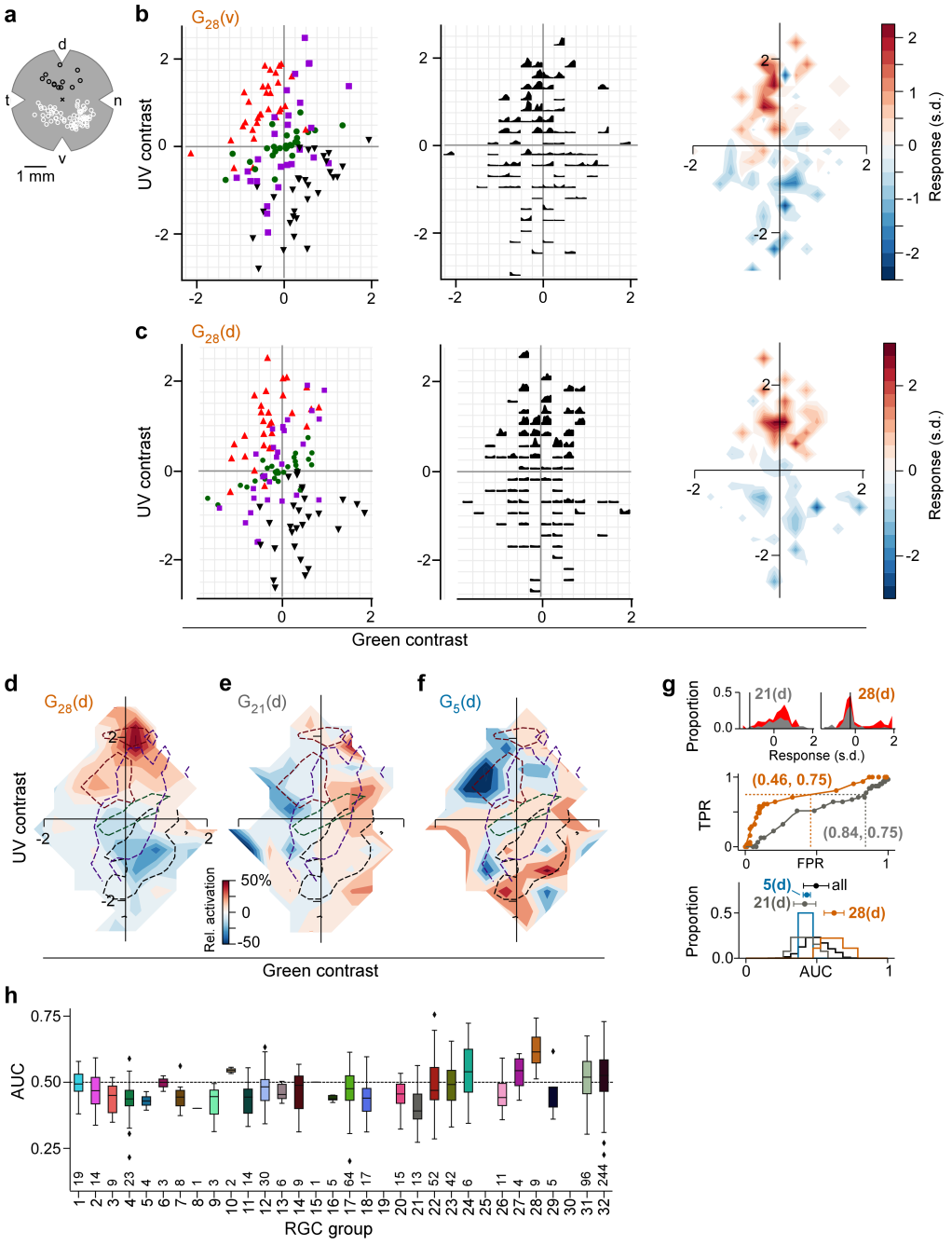

Figure VII 6-figure supplement 2. **(a)** Illustration of a flat-mounted retina, with recording fields in the dorsal (black circles) and ventral (white circles) retina (cross marks optic disc; d, dorsal; v, ventral; t, temporal; n, nasal). **(b)** *Left*: Distribution of green and UV contrasts of N=122 inter-clip transitions seen by a *ventral* group 28 (G_{28}) RGC, coloured by transition type (red triangle, ground-to-sky; green disk, ground-to-ground; black downward triangle, sky-to-ground; purple square, sky-to-sky). *Middle*: Responses of example RGC in the 1 s following an inter-clip transition, averaged across transitions within the bins indicated by the grid. *Right*: Responses transformed into a tuning map by averaging within bins as defined by grid (*Left*. Responses are z-scored ($\mu = 0$, $\sigma = 1$). **(c)** Like (b) but for a *dorsal* G_{28} RGC. **(d)** Tuning map of N=9 *dorsal* G_{28} RGCs, created by averaging the tuning maps of the individual RGCs. **(e)** Same as (d) for N=13 G_{21} RGCs. **(f)** Same as (d) for N=4 G_5 RGCs. **(g)** *Top*: Illustration of ROC analysis for two dorsal RGCs, a G_{21} (left) and a G_{28} (right). For each RGC, responses were binned to all inter-clip transitions, separately for ground-to-sky (red) and all other transitions (grey). *Middle*: Sliding a threshold d across the response range, classifying all transitions with response $> d$ as ground-to-sky, and registering the false-positive-rate (FPR) and true-positive-rate (TPR) for each threshold yields an ROC curve (middle). Numbers in brackets indicate (FPR, TPR) at the threshold indicated by black vertical line in histogram plots. *Bottom*: We evaluated performance for each cell as the area under the ROC curve (AUC), and plotted the distribution across AUC values for all cells (black), for G_5 (blue), for G_{21} (grey), and for G_{28} (orange). Among the dorsal RGCs, G_{28} RGCs achieved the highest AUC on average (mean $\pm$ SD AUC, G_{28} (N=9 cells): 0.62 ± 0.07; all other groups (N=720): 0.49 ± 0.09, $\Delta\text{AUC} = 0.13$, bootstrapped 95% confidence interval $\text{CI}_{95} = [0.08, 0.18]$, Cohen's $d = 1.45$, two-sample permutation test G_{28} vs. all other groups (see Methods): $p = 0$ with 100,000 permutations; next-best performing G_{24} (N=6): 0.54 ± 0.12, $\Delta\text{AUC} = 0.08$, bootstrapped 95% confidence interval $\text{CI}_{95} = [0.01, 0.18]$, Cohen's $d = 0.87$; two-sided t-test G_{28} vs. G_{24}: $p = .15$ with 100,000 permutations (not significant)). AUC mean $\pm$ SD indicated as dots and horizontal lines above histograms. **(h)** Boxplot of AUC distributions per cell type (*dorsal*). The box extends from the first quartile (Q_1) to the third quartile (Q_3) of the data; the line within a box indicates the median. The whiskers extend to the most extreme points still within $[Q_1 - 1.5 \times \text{IQR}, Q_3 + 1.5 \times \text{IQR}]$, IQR = inter-quartile range. Diamonds indicate points outside this range. All elements of the plot (upper and lower boundaries of the box, median line, whiskers, diamonds) correspond to actual observations in the data. Numbers of RGCs for each type are indicated in the plot.

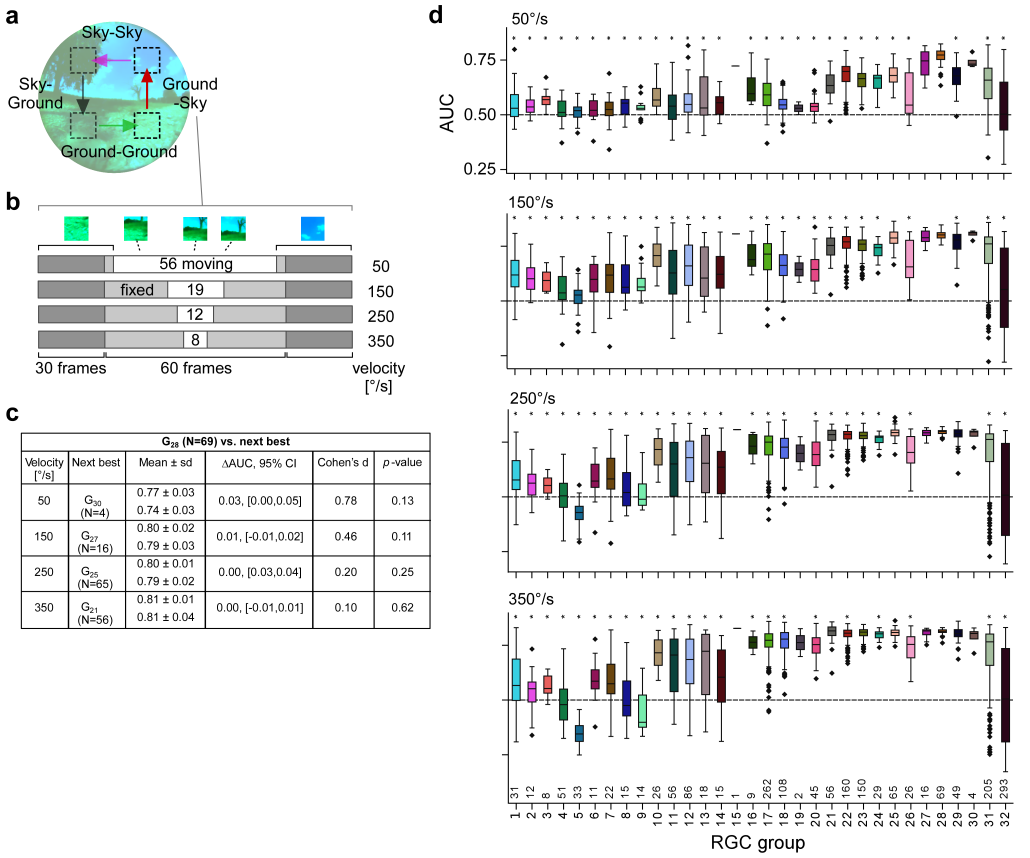

c

G_{28} (N=69) vs. next best					
Velocity [°/s]	Next best	Mean ± sd	ΔAUC, 95% CI	Cohen's d	*p*-value
50	G_{30} (N=4)	0.77 ± 0.03 0.74 ± 0.03	0.03, [0.00,0.05]	0.78	0.13
150	G_{27} (N=16)	0.80 ± 0.02 0.79 ± 0.03	0.01, [-0.01,0.02]	0.46	0.11
250	G_{25} (N=65)	0.80 ± 0.01 0.79 ± 0.02	0.00, [0.03,0.04]	0.20	0.25
350	G_{21} (N=56)	0.81 ± 0.01 0.81 ± 0.04	0.00, [-0.01,0.01]	0.10	0.62

Figure VIII 6-figure supplement 3. (a) Illustration transition stimulus paradigm (from Figure 7h). **(b)** Structure of stimuli for different velocities, using a ground-to-sky transition as an example. **(c)** Statistics of the area under the ROC curve (AUC) for the sky-ground detection task in the simulation for different velocities (G_{28} vs. the next-best RGC group). Columns (from *left*): mean ± standard deviation of AUC values (top: G_{28}; bottom: the respective best next RGC type); difference in mean AUC and corresponding bootstrapped 95% confidence intervals; Cohen's d and *p*-value of a two-sample permutation test with 100,000 repeats. **(d)** Boxplots of AUC distributions per cell type for the different velocities (plots like in Figure 7g,j).